Coulomb and nuclear polarization of the nucleon density in the dinuclear configuration of the ^{40}Ca + ^{208}Pb system

Bakhodir Kayumov *

Department of Physics, New Uzbekistan University, Tashkent 100000, Uzbekistan
and Laboratory of Theoretical Nuclear Physics, Institute of Nuclear Physics, Tashkent 100214, Uzbekistan

(Received 30 July 2026; revised 12 September 2026; accepted 14 October 2026; published 28 October 2026)

The change of the nucleon density distribution of a heavy nucleus caused by the presence of a second nucleus at a fixed center-to-center distance is studied in the framework of the deformed Woods–Saxon mean field. The single-particle problem of one nucleus has been solved by diagonalization in a cylindrical harmonic-oscillator basis with the external field of the partner nucleus included in the Hamiltonian before diagonalization. The external field consists of the Coulomb potential of the partner charge distribution and of the nuclear part obtained by double folding of the Migdal density-dependent effective nucleon-nucleon interaction, in the same form as used in the dinuclear system approach. The induced density change $\delta\rho(\boldsymbol{r};R)$ and the corresponding changes of the quadrupole moment, of the mean-square radius and of the interaction energy have been calculated for the ^{40}Ca + ^{208}Pb system at separations $R = 15.5$–20 fm. The results are compared with the first-order (linear-response) treatment of the same external field. Because the mean field is anchored at the origin, the multipole moments are shown to require a translationally invariant definition: a displaced but undeformed distribution acquires a quadrupole moment second order in the displacement, and in this problem that kinematic term is comparable with the induced moment itself. Once it is removed, the intrinsic quadrupole response of ^{208}Pb agrees with the first-order one to better than half a percent, and remains so over the full range of the switching parameter for the Coulomb field at $R = 20$ fm, while that of ^{40}Ca retains a genuine higher-order contribution of 12% to 16%. The polarization of both partners is dominated by the repulsive Coulomb tidal field, which produces an oblate deformation of the density, while the attractive nuclear field acts in the opposite sense and partially cancels the Coulomb contribution at the smallest separations. At the larger separations the induced octupole deformation is close to 40% of the quadrupole one for ^{208}Pb and to 50% for ^{40}Ca, and it is the more sensitive indicator of the breakdown of the one-center picture. The polarization energy is a dipole quantity, the induced quadrupole deformation contributing only a few percent of it; it is verified by coupling-constant integration and is quoted under several correction prescriptions for the spurious translational component and for the absence of the residual interaction. The sensitivity to the geometry of the folding densities and the limits of validity of the one-center description are established quantitatively.

DOI: 10.1103/d6vs-ppv1

I. INTRODUCTION

The synthesis of superheavy elements and the study of the fusion-fission dynamics of massive nuclear systems remain among the active topics of low-energy nuclear physics [1,2]. In the entrance channel of such reactions, the two nuclei approach each other under the combined action of the Coulomb repulsion and of the nuclear attraction, and at distances close to the touching configuration they form a dinuclear system (DNS) which evolves in mass and charge asymmetry [3,4]. The theoretical description of this stage requires the nucleus-nucleus interaction potential, the driving potential and the single-particle level scheme of the two-center system [5–7]. In the DNS approach, all of these quantities are constructed from the ground-state densities of the two nuclei, which are kept frozen during the approach, and the deformation parameters entering them are the static ones taken from the tables [8,9]. The polarization of the densities by the field of the partner is not taken into account in the equations of relative motion, and the size of the correction which is thereby neglected has not been established microscopically.

This assumption is convenient, but it is not exact. Each nucleus is a polarizable object, and the field created by the partner modifies its single-particle wave functions and therefore its density distribution. It is well known that the polarization of the nuclear surface influences the height and position of the Coulomb barrier and the value of the nucleus-nucleus potential in the region of the potential pocket [10].

The frozen-density approximation has been examined from several directions. In the double-folding model, the interaction

*Contact author: b.kayumov@newuu.uz

Published by the American Physical Society under the terms of the Creative Commons Attribution 4.0 International license. Further distribution of this work must maintain attribution to the author(s) and the published article's title, journal citation, and DOI.

potential is obtained by folding the ground-state densities of the two nuclei with an effective nucleon-nucleon interaction [11], and the generalized version of the model with a density-dependent M3Y force reproduces elastic and inelastic nucleus-nucleus scattering over a wide range of systems [12]. The same construction, with the Migdal density-dependent interaction, provides the nucleus-nucleus potential of the DNS approach [4,8]. In all of these treatments, the densities entering the folding integral are those of the isolated nuclei. The frozen Hartree-Fock method makes the same assumption within a self-consistent mean field, the two colliding nuclei keeping their ground-state densities at every separation, and it has been used extensively to construct bare interaction potentials and to study the role of the Pauli principle in the barrier region.

Fully dynamical microscopic descriptions relax this assumption. The time-dependent Hartree-Fock (TDHF) theory follows the self-consistent evolution of the single-particle wave functions of the whole system and therefore contains the dynamical polarization of both partners automatically, together with neck formation, nucleon transfer and one-body dissipation [13,14]. Interaction potentials extracted from TDHF by the density-constrained method (DC-TDHF) [15] and by the method of Washiyama and Lacroix [16] show explicitly where the frozen-density picture ceases to apply. It was found in Ref. [16] that at center-of-mass energies well above the Coulomb barrier the microscopic potential coincides with the frozen-density one, whereas on approaching the barrier the potential becomes energy dependent, the barrier is lowered and its position moves outwards. This energy dependence is the signature of the rearrangement of the internal degrees of freedom which the frozen-density approximation omits.

These approaches establish that dynamical polarization is present and that it matters near the barrier, but they do not by themselves answer the question which is relevant for the DNS approach. In TDHF and DC-TDHF, the polarization is inseparable from the other processes which occur simultaneously, and the quantity which is obtained is the potential of the combined system rather than the density change of one of the partners. The response of a given nucleus to the field of the other one, decomposed into its Coulomb and nuclear parts and expressed through the multipole moments which enter the DNS driving potential, is not directly accessible in that way. Microscopic studies of induced polarization have also been carried out in the linear-response and random-phase approximations, mainly for the electromagnetic response and for the polarization potential in elastic scattering [17,18], but not with the nuclear part of the external field constructed from the same effective interaction that generates the DNS potential.

The present work addresses this gap. The density change of one nucleus produced by the static external field of its partner is calculated explicitly; the Coulomb and nuclear contributions are separated, and the nuclear part is obtained by double folding of the Migdal interaction in exactly the form in which it is used in the DNS approach, so that the correction is compatible with the potential which governs the relative motion. The result is expressed through the induced multipole moments and the polarization energy, which are the quantities entering the DNS driving potential and the equations of relative motion, and a quantitative criterion is established for the range of separations in which the description of one nucleus in the fixed field of the other remains meaningful.

The advantages and limitations of this approach with respect to the fully dynamical methods should be stated clearly. It is a static calculation with a frozen partner, so that neck formation, nucleon transfer and dissipation are absent, and the response is obtained at the level of the unperturbed particle-hole spectrum without the residual interaction. TDHF and DC-TDHF contain all of these effects and are therefore superior as descriptions of the collision. On the other hand, the present treatment isolates one well-defined quantity, the density change of a single nucleus in a specified external field, which the dynamical methods do not provide separately; it allows the Coulomb and nuclear parts of the polarization to be examined independently; and it uses the same effective interaction and the same geometry as the DNS calculations, so that the result can be carried over to them without a change of framework. It is intended as a source of microscopic corrections to the DNS entrance channel, not as a substitute for a dynamical description of the collision.

The purpose of the present work is to calculate the density change

$$\delta\rho(\boldsymbol{r};R) = \rho(\boldsymbol{r};R) - \rho_0(\boldsymbol{r}), \tag{1}$$

where ρ_0 is the ground-state density of the isolated nucleus and $\rho(\boldsymbol{r};R)$ is its density in the presence of the partner nucleus placed at the center-to-center distance R, and to obtain from it the induced multipole moments and the polarization energy. The single-particle problem is solved with the axially deformed Woods–Saxon potential of Ćwiok *et al.* [19], in which the external field of the partner has been included as an additional local term of the Hamiltonian. The nuclear part of the external field is calculated by double folding of the Migdal density-dependent effective interaction, which is the same interaction that is used to construct the nucleus-nucleus potential in the DNS approach [8,20]. The $^{40}\mathrm{Ca} + {}^{208}\mathrm{Pb}$ system has been chosen because both partners are doubly magic and spherical in their ground states, so that any deformation of the density is entirely induced by the partner, and because this system has been studied extensively as a reference case for quasifission and deep-inelastic processes. The restriction to spherical partners is deliberate. It removes the static deformation of the ground state from the problem and allows the induced polarization to be identified without ambiguity, which is necessary in order to establish the method and its limits. The formalism presented below is not restricted to spherical shapes, and the extension to statically deformed nuclei, where the orientation of the symmetry axes relative to the internuclear axis becomes an additional degree of freedom, is left to a subsequent work.

The choice of the effective interaction which generates the external nuclear field deserves particular attention. In the DNS approach, the folded potential is used as the interaction energy between two nuclei, and its range is governed by the overlap of the two density distributions. If the same expression is replaced by a Woods–Saxon well whose radius is taken as the

sum of the two nuclear radii, which is a natural parametrization of the nucleus-nucleus potential as a function of R, the resulting field acting on a single nucleon extends over a region much larger than the partner nucleus itself. Such a field does not represent the interaction of one nucleon with the nucleus B and, as shown in Sec. III, it destroys the one-center description at separations where the two nuclei are still well separated. The distinction between a nucleus-nucleus interaction radius and the range of a single-nucleon field is therefore essential in this type of calculation.

Two different treatments of the external field are compared. In the first one, the field is added to the mean-field Hamiltonian and the eigenvalue problem is solved again, so that the response is obtained to all orders in the external field. In the second one, the density change is evaluated in first-order perturbation theory, which is the standard linear-response expression. The comparison of the two provides a direct measure of the importance of the higher-order terms and, at the same time, an internal test of the calculations.

It should be stressed that the description of one nucleus in the fixed field of another one is meaningful only as long as the two nuclei retain their individuality. When the external field becomes strong enough to bind a nucleon in the region of the partner, the single-particle states of the combined system are no longer localized in one of the nuclei, and the notion of the density of a single nucleus loses its meaning. The conditions under which this happens are examined quantitatively in the present work, and a simple criterion for the applicability of the one-center description is proposed.

This paper is structured as follows: Sec. II presents the theoretical framework, the external field and the two methods used to obtain the density change; Sec. III discusses the range of validity of the one-center picture; Sec. IV presents the results for the $^{40}\mathrm{Ca} + {}^{208}\mathrm{Pb}$ system. Finally, the conclusions are reported in Sec. V.

II. THEORETICAL FRAMEWORK

A. Single-particle Hamiltonian of the isolated nucleus

The single-particle states of the isolated nucleus are obtained from the axially symmetric Woods–Saxon Hamiltonian

$$\hat{h}_0 = \hat{t} + V_{\mathrm{WS}}(\boldsymbol{r}) + V_{\mathrm{so}}(\boldsymbol{r}) + V_{\mathrm{C}}(\boldsymbol{r}), \tag{2}$$

where $\hat{t}$ is the kinetic-energy operator, V_{WS} is the central Woods–Saxon term, V_{so} is the spin-orbit term, and V_{C} is the Coulomb potential of the nucleus itself, acting on protons only. The central term is written as

$$V_{\mathrm{WS}}(\boldsymbol{r}) = \frac{V_0}{1 + \exp\left[\mathrm{dist}(\boldsymbol{r}, \Sigma)/a\right]}, \tag{3}$$

$$V_0 = -V_{00}\left(1 \pm \kappa \frac{N-Z}{A}\right), \tag{4}$$

where $\mathrm{dist}(\boldsymbol{r}, \Sigma)$ is the distance from the point $\boldsymbol{r}$ to the nuclear surface Σ, a is the diffuseness parameter, and the upper and lower signs refer to protons and neutrons, respectively. The parameters used in the present calculations are those of the Rost set as implemented in Ref. [19]: $V_{00} = 49.6$ MeV, $\kappa = 0.86$ and $a = 0.70$ fm, with the central radius parameter $r_0 = 1.347$ fm for neutrons and 1.275 fm for protons, and the spin-orbit parameters $r_{0,\mathrm{so}} = 1.280$ and 0.932 fm and $\lambda_{\mathrm{so}} = 31.5$ and 17.8 for neutrons and protons, respectively. For ^{208}Pb this gives well depths of -40.6 MeV for neutrons and -58.6 MeV for protons before the Coulomb term is added.

The eigenvalue problem for $\hat{h}_0$ is solved by diagonalization in the basis of the axially deformed harmonic oscillator, in cylindrical coordinates (ρ, z, φ),

$$\phi_\alpha(\rho, z, \varphi) = \varphi_{n_z}\left(\frac{z}{b_z}\right)\varphi^{\Lambda}_{n_\rho}\left(\frac{\rho}{b_\rho}\right)\frac{e^{i\Lambda\varphi}}{\sqrt{2\pi}}\chi_\sigma, \tag{5}$$

where φ_{n_z} and $\varphi^{\Lambda}_{n_\rho}$ are the normalized Hermite and Laguerre functions, χ_σ is the spin function, and the oscillator lengths are

$$b_z = \frac{\hbar c}{\sqrt{mc^2\hbar\omega_z}}, \quad b_\rho = \frac{\hbar c}{\sqrt{mc^2\hbar\omega_\rho}}. \tag{6}$$

The oscillator frequency is taken as $\hbar\omega_0 = \lambda \times 41A^{-1/3}$ MeV with the basis scaling factor $\lambda = 1.2$. The nuclear surface Σ entering Eq. (3) is parametrized by the multipole deformation parameters $\beta_2, \beta_3, \ldots, \beta_6$, so that the mean field admits axially deformed shapes; in the present work all of them are set to zero, since both nuclei considered are spherical in their ground states. Since the Hamiltonian is invariant under rotations about the symmetry axis and under time reversal, the matrix is block diagonal in the projection Ω of the total angular momentum on the symmetry axis and in the parity π, and only the blocks with $\Omega > 0$ have to be diagonalized. Every level obtained in this way is twofold degenerate, the two members of the Kramers doublet corresponding to $\pm\Omega$. The basis has been truncated at $N_{\max} = 15$ oscillator shells, which gives 816 single-particle states for each isospin.

B. External field of the partner nucleus

The partner nucleus B is placed on the symmetry axis of the nucleus A under study, at $z = R$. This choice preserves the axial symmetry of the problem and keeps Ω a good quantum number. The distance from a point (ρ, z) to the center of B is

$$d(\rho, z; R) = \sqrt{\rho^2 + (z - R)^2}. \tag{7}$$

The external field is the sum of a Coulomb and a nuclear part,

$$U_{\mathrm{ext}}(\boldsymbol{r}; R) = U_{\mathrm{C}}^{(B)}(\boldsymbol{r}; R) + U_{\mathrm{N}}^{(B)}(\boldsymbol{r}; R), \tag{8}$$

the Coulomb part acting on protons only.

1. Coulomb part

The Coulomb field created by the charge distribution of B is calculated in the uniformly charged sphere approximation,

$$U_{\mathrm{C}}^{(B)}(d) = \begin{cases} \frac{Z_B e^2}{d}, & d > R_B^{\mathrm{ch}} \\ \frac{Z_B e^2}{2R_B^{\mathrm{ch}}}\left(3 - \frac{d^2}{(R_B^{\mathrm{ch}})^2}\right), & d \leqslant R_B^{\mathrm{ch}}, \end{cases} \tag{9}$$

with $R_B^{\mathrm{ch}} = 1.2A_B^{1/3}$ fm. At the separations considered here, the whole volume of the nucleus A lies outside the charge

distribution of B, so that only the first line of Eq. (9) is effective. The multipole expansion of the point-charge field about the center of A gives

$$U_{\rm C}^{(B)}(\boldsymbol{r}) = \frac{Z_B e^2}{R} \sum_{\lambda} \left(\frac{r}{R}\right)^{\lambda} P_{\lambda}(\cos\theta), \tag{10}$$

so that the term which drives the quadrupole polarization has the strength $Z_B e^2/(2R^3)$ and falls off as R^{-3}. This tidal behavior is used below as a test of the calculations.

2. Nuclear part

The nuclear part of the external field is obtained by folding the density of the partner nucleus with the effective nucleon-nucleon interaction. The Migdal density-dependent zero-range force is used,

$$v_{\rm eff}(\boldsymbol{r}_1, \boldsymbol{r}_2) = C_0 \left[f'_{\rm ex} + f''_{\rm in} \frac{\rho(\boldsymbol{r}_1)}{\rho_0} \right] \delta(\boldsymbol{r}_1 - \boldsymbol{r}_2), \tag{11}$$

where $\rho = \rho_A + \rho_B$ is the total nucleon density at the point of interaction, $\rho_0 = 0.17$ fm^{-3} is the saturation density and $C_0 = 300$ MeV fm^3. The isospin dependence enters through

$$f'_{\rm ex} = f_{\rm ex} + f^1_{\rm ex}\xi, \quad f''_{\rm in} = f_{\rm in} + f^1_{\rm in}\xi - f'_{\rm ex}, \tag{12}$$

with $\xi = [(2Z_A - A_A)/A_A][(2Z_B - A_B)/A_B]$ and the parameter values $f_{\rm in} = 0.09$, $f_{\rm ex} = -2.59$, $f^1_{\rm in} = 0.42$ and $f^1_{\rm ex} = 0.54$ [8,20]. These are the same interaction and the same parameter set that are used to construct the nucleus-nucleus potential in the DNS approach, so that the external field employed here is consistent with the potential which governs the relative motion. It should be noted that for the ^{40}Ca + ^{208}Pb system the isospin factor ξ vanishes because ^{40}Ca has $N = Z$, and therefore $f'_{\rm ex} = -2.59$ and $f''_{\rm in} = 2.68$.

Folding Eq. (11) with the two densities gives the nucleus-nucleus potential

$$V_{\rm N}(R) = C_0 \int \rho_A(\boldsymbol{r}) \rho_B(\boldsymbol{r} - \boldsymbol{R}) \left[f'_{\rm ex} + f''_{\rm in} \frac{\rho_A + \rho_B}{\rho_0} \right] d^3r. \tag{13}$$

The field acting on a single nucleon of A is the functional derivative of Eq. (13) with respect to ρ_A,

$$U_{\rm N}^{(B)}(\boldsymbol{r}; R) = \frac{\delta V_{\rm N}}{\delta \rho_A(\boldsymbol{r})} = C_0 \rho_0 \hat{\rho}_B [f'_{\rm ex} + f''_{\rm in}(2\hat{\rho}_A + \hat{\rho}_B)], \tag{14}$$

where $\hat{\rho}_i = \rho_i/\rho_0$ and the term proportional to $\hat{\rho}_A$ is the rearrangement contribution arising from the density dependence of the force. The densities are taken in the two-parameter Fermi form with the effective radii used in the DNS calculations,

$$R_i = c_i \sqrt{\frac{R_p^2 Z_i + R_n^2 (A_i - Z_i)}{A_i}}, \tag{15}$$

with $R_p = 1.237(1 - 0.157\delta_i - 0.646/A_i)A_i^{1/3}$, $R_n = 1.176(1 + 0.25\delta_i + 2.806/A_i)A_i^{1/3}$, $\delta_i = (A_i - 2Z_i)/A_i$, and diffuseness $a_0 = 0.54$ fm. The values obtained are $R = 3.97$ fm for ^{40}Ca and $R = 7.03$ fm for ^{208}Pb. Since both nuclei considered here are spherical, the radii of Eq. (15) do not depend on the direction. In the general case, the surface of the partner is written as $R_i(\theta) = R_i[1 + \sum_\lambda \beta_{\lambda i} Y_{\lambda 0}(\theta)]$ and the folding acquires a dependence on the orientation angles of the two symmetry axes with respect to the internuclear axis, in the same way as in the calculation of the nucleus-nucleus potential in the DNS approach [4]. The external field then loses its axial symmetry unless both nuclei are oriented along the internuclear axis, and Ω ceases to be a good quantum number for arbitrary orientations.

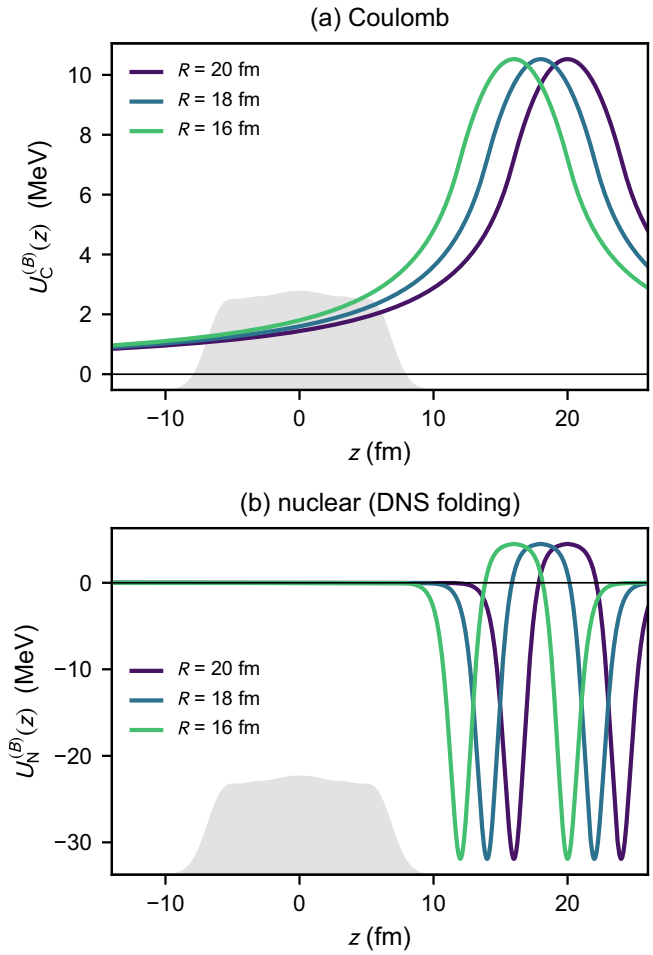


FIG. 1. Coulomb (a) and nuclear (b) components of the external field created by ^{40}Ca along the symmetry axis, for three center-to-center distances. The shaded area shows the ground-state density of ^{208}Pb on an arbitrary scale. The nuclear component follows the density of the partner and does not extend into the volume of ^{208}Pb.

Because the force of Eq. (11) has zero range, the external field of Eq. (14) follows the density of the partner directly and has no tail beyond it. This property is essential for the applicability of the whole approach and is discussed in Sec. III. It is also important to note that the Migdal force is repulsive at saturation density, $f_{\rm in} > 0$, so that $U_{\rm N}^{(B)}$ is positive at the center of the partner and reaches its largest attractive value, about -32 MeV, in the surface region of B. The behavior of the two components of the external field along the symmetry axis is shown in Fig. 1 for three separations, together with the density profile of ^{208}Pb.

C. Nonperturbative treatment

In the first method, the external field is added to the mean-field Hamiltonian,

$$\hat{h} = \hat{h}_0 + \lambda U_{\rm ext}(\boldsymbol{r}; R), \tag{16}$$

where the switching parameter $\lambda \in [0, 1]$ is introduced in order to test the linearity of the response, and the eigenvalue problem is solved again in the same oscillator basis. The field of Eq. (8) is evaluated on the Gauss–Hermite and Gauss–Laguerre mesh used for the matrix elements of the Woods–Saxon potential, so that no additional approximation is introduced in the construction of the Hamiltonian matrix.

Since the partner nucleus is located at $z = R$, the external field is not invariant under the reflection $z \to -z$, and parity is no longer a good quantum number. The blocks of the Hamiltonian matrix corresponding to the two parities of a given Ω are therefore merged and diagonalized together, so that only Ω remains a good quantum number in the perturbed problem. If this is not done, the calculation responds to the mirror image $U_{\rm ext}(-|z|)$ of the true field, and all odd multipole moments of $\delta\rho$ vanish identically.

D. Linear response

In the second method the density change is obtained in first order in $U_{\rm ext}$ from the unperturbed eigenstates,

$$\delta\rho(\boldsymbol{r}; R) = \sum_{ph} \frac{\langle p|U_{\rm ext}|h\rangle}{\varepsilon_h - \varepsilon_p} \phi_p^*(\boldsymbol{r})\phi_h(\boldsymbol{r}) + \text{c.c.}, \tag{17}$$

where h and p label occupied and empty single-particle states of $\hat{h}_0$. The corresponding change of any one-body observable $\hat{F}$ is

$$\Delta F = 2g \sum_{ph} \frac{\langle p|U_{\rm ext}|h\rangle\langle p|\hat{F}|h\rangle}{\varepsilon_h - \varepsilon_p}, \tag{18}$$

with $g = 2$ the Kramers degeneracy. Both $U_{\rm ext}$ and the multipole operators are axially symmetric and spin independent, so that they conserve Ω and the sum in Eq. (18) runs inside each Ω block. The matrix elements are evaluated by Gauss–Legendre quadrature in the same oscillator basis. The residual interaction is not included, so that Eq. (17) corresponds to the independent-particle response χ_0; the random-phase approximation would replace it by $\delta\rho = (1 - \chi_0\hat{f})^{-1}\chi_0 U_{\rm ext}$ [21].

The linear-response expression is built on the unperturbed states and therefore cannot become unstable, whatever the strength of the external field. Its accuracy, on the other hand, is limited to the region where the response is actually linear. The comparison of Eqs. (18) and (16) presented in Sec. IV shows where this condition is satisfied.

E. Occupation numbers and observables

The occupation numbers are obtained from the BCS equations with a constant pairing strength $G = 18$ MeV fm^3. Since only the $\Omega > 0$ blocks are computed, the number equation reads $N = 2\sum_i v_i^2$, while the gap equation is a sum over Kramers doublets and carries no such factor. For the doubly magic nuclei considered here, the pairing gap collapses, and the occupation reduces to the sharp filling of the lowest $N/2$ levels. The density is then

$$\rho(\rho, z) = 2\sum_i v_i^2 |\psi_i(\rho, z)|^2, \tag{19}$$

where the two (Λ, σ) channels contained in each Ω block are summed incoherently, since they differ in the $e^{i\Lambda\varphi}$ factor and in the spinor component.

From $\delta\rho$ the following quantities are obtained,

$$\delta A = \int \delta\rho d^3r \simeq 0, \tag{20}$$

$$\Delta\langle r^2\rangle = \frac{1}{A}\int r^2\delta\rho d^3r, \tag{21}$$

$$\Delta Q_{20} = \int (2z^2 - x^2 - y^2)\delta\rho d^3r, \tag{22}$$

$$\Delta D_1 = \int z\delta\rho d^3r, \tag{23}$$

$$\Delta E = \frac{1}{2}\int U_{\rm ext}\delta\rho d^3r, \tag{24}$$

the first of which serves as a check of the numerical accuracy. A positive ΔQ_{20} corresponds to a prolate elongation of the density along the internuclear axis and a negative one to an oblate compression.

F. Translational invariance of the induced moments

The mean field is anchored at the origin, so that the moments of Eqs. (22) and (23) are referred to a fixed point and not to the density itself. If a distribution of N_q particles is displaced rigidly by d along the symmetry axis, the parallel-axis theorem gives

$$Q_{20}(\text{origin}) = Q_{20}(\text{own centroid}) + 2N_q d^2, \tag{25}$$

that is, a displaced but undeformed density acquires a quadrupole moment of second order in the displacement. The external field does displace the protons of A with respect to the fixed center, so that this term is present in every moment taken about the origin, and it is a property of the coordinate system and not of the shape. The first-order linear response of Eq. (18) contains the displacement but not its square, whereas the rediagonalization contains both, so that a comparison of the two in the laboratory frame would ascribe a purely kinematic difference to a nonlinear response.

Two translationally invariant moments are therefore used. Each of them is the difference between the moment of the perturbed density about its own centroid and the moment of the unperturbed density about its centroid. This is not the same as the shifted operator integrated against $\delta\rho$, which would give $\Delta Q_{20} - 4D_1^2/A$, since $\bar{z}$ is itself of first order in the field. Referring the total density to its center of mass (c.m.) $\bar{z} = D_1/A$, and each isospin species to its own centroid $\bar{z}_q = D_1^{(q)}/N_q$, gives

$$\Delta Q_{20}^{\rm c.m.} = \Delta Q_{20} - \frac{2D_1^2}{A}, \quad \Delta Q_{20}^{\rm sh} = \Delta Q_{20} - 2\sum_{q=n,p}\frac{\left(D_1^{(q)}\right)^2}{N_q}, \tag{26}$$

where $\int \delta\rho d^3r = 0$ and $\int z\delta\rho d^3r = D_1$ have been used. The three moments differ by

$$\Delta Q_{20} = \underbrace{\Delta Q_{20}^{\rm sh}}_{\text{shape}} + \underbrace{\frac{2N_nN_p}{A}d_{\rm rel}^2}_{n\text{-}p\ \text{offset}} + \underbrace{\frac{2D_1^2}{A}}_{\text{translation}}, \tag{27}$$

with $d_{\rm rel} = \bar{z}_p - \bar{z}_n$. The first term is a genuine deformation; the second is the mass quadrupole of two mutually displaced but undeformed distributions, which is a real property of the polarized nucleus; and the third is the displacement of the nucleus as a whole against the anchored field, which has no physical counterpart. The moments quoted in Sec. IV are those of $\Delta Q_{20}^{\rm c.m.}$, which retains the first two of them, while the comparison with the linear response uses $\Delta Q_{20}^{\rm sh}$ for both treatments, since this is the quantity returned by the first-order expression.

The octupole moment is constructed in the same way, as a difference of moments each of which is taken about the centroid of its own density, with the operator

$$P_3(\boldsymbol{r}) = \tfrac{1}{2}\left(5z^3 - 3zr^2\right) = \tfrac{1}{2}\left(2z^3 - 3z\rho_\perp^2\right) = r^3P_3(\cos\theta), \tag{28}$$

where $\rho_\perp^2 = x^2 + y^2$. It has no compact closed form in terms of D_1 and is evaluated numerically; the corresponding deformation parameters are given in Eq. (33). For the dipole, the invariant combination is the one obtained with the $E1$ effective charges $q_p = N/A$ and $q_n = -Z/A$,

$$\Delta D_1^{E1} = \frac{N}{A}\Delta D_1^{(p)} - \frac{Z}{A}\Delta D_1^{(n)}, \tag{29}$$

which measures the displacement of the protons relative to the neutrons and not relative to the origin.

G. Numerical accuracy

Several tests have been performed in order to control the numerical accuracy of the calculations. The densities are evaluated on a mesh covering $|z| \leqslant 16$ fm and $\rho \leqslant 13$ fm with 100×70 points, which is sufficient to conserve the integrated particle number to better than 10^{-4} for $A = 208$; a smaller box truncates the tail of the density and loses about 0.7% of the nucleons. The matrix elements entering Eq. (18) are evaluated with 220×130 Gauss–Legendre points, for which the orthonormality of the 816 single-particle states is satisfied to 7×10^{-6}. The quadrupole moment of the isolated ^{208}Pb, which must vanish for a closed-shell nucleus, is obtained as 0.04 fm^2 with that quadrature. On the coarser mesh used for the densities themselves, it is -1.14 fm^2 for ^{208}Pb and -0.23 fm^2 for ^{40}Ca, which is the error of representing a sphere on a cylindrical grid of this spacing. That offset does not propagate into the results, because the induced moments are differences of two integrals evaluated on the same mesh and it cancels between them. This cancellation can be verified directly. For ^{40}Ca at $\lambda = 0.1$ the induced moment, -0.144 fm^2, is smaller in magnitude than the offset itself, and nevertheless it agrees to 1.5% with the first-order value obtained from the independent Gauss–Legendre quadrature.

The dependence of the results on the size of the oscillator basis has been examined by repeating the calculations with

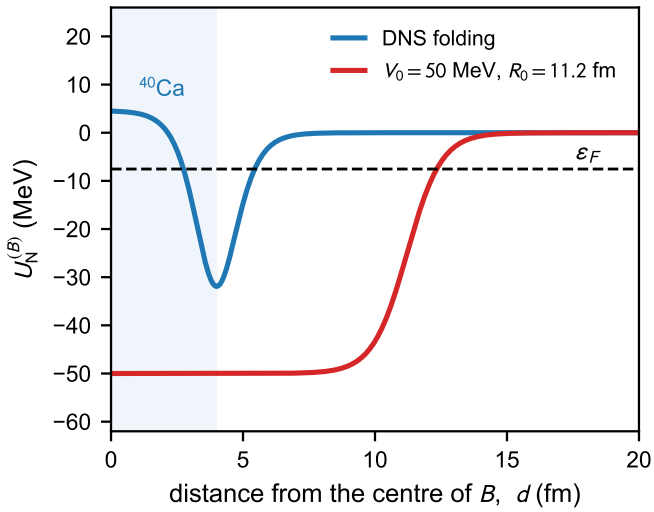


FIG. 2. Nuclear part of the external field of ^{40}Ca as a function of the distance to its center, obtained from the folding of Eq. (14) and from a Woods–Saxon well whose radius is taken as the sum of the two nuclear radii, $R_0 = 1.2(A_A^{1/3} + A_B^{1/3}) = 11.2$ fm. The shaded band indicates the extent of the ^{40}Ca density and the dashed line the Fermi energy of ^{208}Pb.

$N_{\rm max} = 10$, 12, and 15. In the range of separations where the one-center description is applicable, the induced quadrupole moment is stable to within 2%. The behavior outside this range is discussed in the next section.

III. VALIDITY OF THE ONE-CENTER DESCRIPTION

Before presenting the results, it is necessary to establish the range of separations in which the calculation of one nucleus in the field of the other is meaningful. The oscillator basis of Eq. (5) is centered on the nucleus A and extends up to $z_{\rm max} \simeq b_z\sqrt{2N_{\rm max} + 3} = 12.8$ fm for $N_{\rm max} = 15$. If the external field is attractive enough within this region, the variational solution places amplitude in the well of the partner. The corresponding states are deeply bound, and since the occupation is determined by the energy ordering, they become occupied. The calculation then describes the combined system rather than the polarized nucleus A.

Figure 3(a) shows the total single-particle potential along the symmetry axis; that is, the Woods–Saxon well of ^{208}Pb plus the external field of ^{40}Ca. For $R \gtrsim 16$ fm a barrier separates the two wells and rises above the Fermi level. Below $R \simeq 15$ fm this barrier disappears, the two wells merge, and the single-particle states are no longer localized in one of the nuclei. The top of the barrier falls below ε_F at $R \simeq 15.3$ fm.

The onset of this behavior is monitored by the number of nucleons which appear beyond the surface of the nucleus A,

$$\Delta N_{\rm leak} = \int_{z>z_s} \rho(\boldsymbol{r}; R)d^3r - \int_{z>z_s} \rho_0(\boldsymbol{r})d^3r, \tag{30}$$

with $z_s = 10$ fm for ^{208}Pb. This quantity is shown in Fig. 3(b). It stays below 10^{-3} down to $R = 17$ fm, reaches 2×10^{-2} at $R = 15.5$ fm and then rises by more than an order of magnitude per fm. The tolerance adopted here is $\Delta N_{\rm leak} = 0.05$

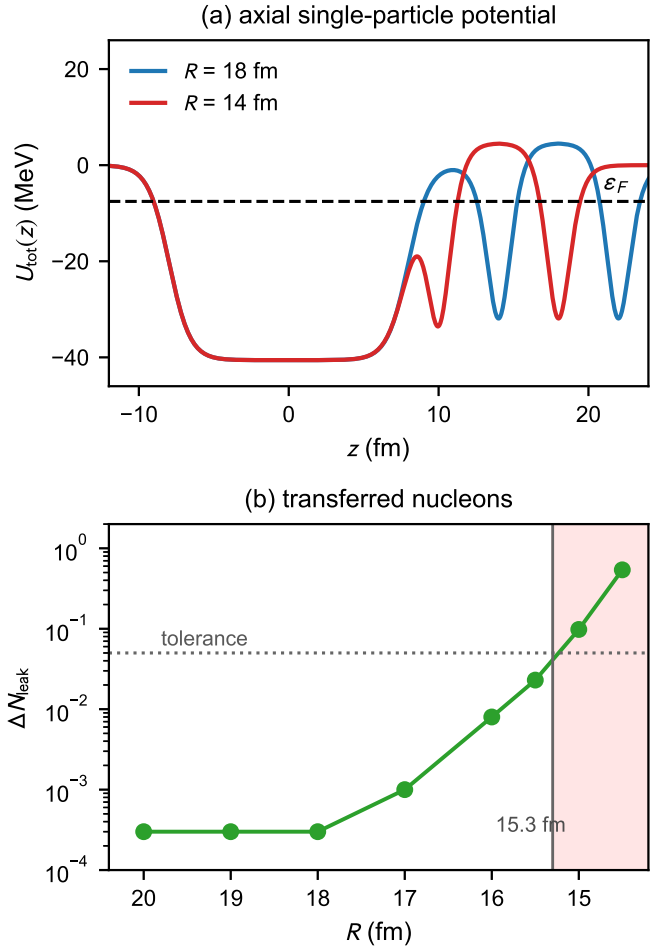


FIG. 3. (a) Total single-particle potential of ^{208}Pb along the symmetry axis in the external field of ^{40}Ca. At $R = 18$ fm a barrier rising above the Fermi energy separates the two wells; at $R = 14$ fm the wells have merged, and no such barrier remains. The double minimum of the partner well reflects the repulsive character of the Migdal force at saturation density. (b) Number of nucleons transferred beyond $z_s = 10$ fm as a function of the separation. The dotted line is the tolerance adopted in this work and the shaded area marks the region in which the one-center description fails.

nucleons, which is crossed at $R \simeq 15.3$ fm; the precise value of the tolerance is immaterial, since the quantity rises so steeply that any choice between 10^{-2} and 10^{-1} moves the limit by less than 0.3 fm. The two criteria are independent, the first being a property of the potential alone and the second of the resulting wave functions, and they locate the breakdown at the same separation.

A calculation that has entered this regime does not converge with the size of the basis. This has been verified for a case in which the external field is deliberately taken in the form of a wide Woods–Saxon well of depth 50 MeV and radius $1.2(A_A^{1/3} + A_B^{1/3})$; that is, with the geometry of a nucleus-nucleus interaction potential rather than of a single-nucleon field. At $R = 20$ fm the induced quadrupole moment grows monotonically from 248 to 687 and 2466 fm^2 as $N_{\rm max}$ is increased from 10 to 12 and 15, whereas at $R = 26$ fm it remains stable at -3.1 fm^2 for the same three basis sizes. The absence of convergence is the signature of a variational collapse: a larger basis reaches further into the well of the partner, lowers the energy, and transfers more nucleons. A result obtained in this regime is therefore not defined independently of the basis, whereas in the range retained in this work the induced moments are stable to within 2% over the same range of $N_{\rm max}$.

The geometry assumed for the external nuclear field determines where this limit lies. Figure 2 compares the folded field of Eq. (14) with a Woods–Saxon well of depth 50 MeV and radius $1.2(A_A^{1/3} + A_B^{1/3}) = 11.2$ fm. The folded field is confined to the density of the partner and falls below the Fermi energy already at $d \simeq 6$ fm, whereas the wide well remains 50 MeV deep out to 10 fm and therefore reaches the surface of ^{208}Pb even when the two centers are 20 fm apart. Applying the criterion of Eq. (31) to the two fields gives $R > 15.3$ fm for the folded one and $R > 22.3$ fm for the wide well, so that the two limits differ by 7 fm. It is therefore the range of the external field, and not its depth, which controls the applicability of the one-center picture.

These observations lead to a simple criterion. The one-center description is applicable as long as the two single-particle wells remain separated by a barrier which lies above the Fermi level; that is, as long as

$$\max_{0<z<z_{\rm min}} [V_{\rm WS}(z) + U_{\rm ext}(z;R)] > \varepsilon_F, \tag{31}$$

where ε_F is the Fermi energy of the nucleus A and $z_{\rm min}$ is the position of the near-side minimum of the partner well. The maximum has to be taken for the neutrons, which are the limiting case, since for the protons the Coulomb field of B adds a repulsive term and the barrier is higher. Evaluated for the ^{40}Ca + ^{208}Pb system with the folded field of Eq. (14), the barrier top falls from -1.01 MeV at $R = 18$ fm to -2.23, -4.82 and -7.00 MeV at $R = 17$, 16, and 15.5 fm, crossing $\varepsilon_F = -7.54$ MeV at $R \simeq 15.3$ fm. The same construction applied to the wide Woods–Saxon well gives $R > 22.3$ fm. The limit obtained in this way agrees with the rise of $\Delta N_{\rm leak}$ in Fig. 3(b) to better than 0.2 fm, although the two diagnostics use different information: the first the potential alone and the second the resulting wave functions. All results presented below have been obtained in this range.

A simpler estimate, which requires no calculation, is obtained by requiring that the external field alone be unable to bind a nucleon at the surface of A, $|U_{\rm ext}(z_s)| < |\varepsilon_F|$ with $z_s \simeq R_A + 2a_0$. For the folded field this gives $R > 13.4$ fm and for the wide well $R > 20.5$ fm. It is the weaker condition of the two, because it omits the contribution of the tail of the Woods–Saxon well of A itself to the barrier, and it is quoted here only as a rule of thumb; the limits used in this work are those of Eq. (31).

It is important to note that the limit is a physical one and not a numerical artifact. The touching configuration of ^{40}Ca + ^{208}Pb corresponds to $R \simeq 12.1$ fm, so that the interval between 12.1 and 15.3 fm is not accessible to any one-center frozen calculation. In this region the two nuclei genuinely share single-particle states, and a two-center basis is required.

TABLE I. Ground-state properties of the isolated nuclei obtained in the present calculation, in comparison with the experimental data. The calculated charge radius is obtained by folding the point-proton distribution with the proton charge form factor, $\langle r^2\rangle_{\rm ch} = \langle r^2\rangle_p + 0.769$ fm^2, and is compared with the measured value of Ref. [22]; the point-nucleon (matter) radius is given separately because it is the quantity entering the folding. The central densities are the values deduced from elastic electron scattering [23] converted to nucleon density, and the Fermi energies are compared with the one-nucleon separation energies of Ref. [24] taken with the opposite sign.

	^{208}Pb		^{40}Ca	
	Calc.	Expt.	Calc.	Expt.
A (integrated)	207.94	208	39.97	40
$\langle r^2\rangle_{\rm ch}^{1/2}$ (fm)	5.52	5.50	3.55	3.48
$\langle r^2\rangle_{p}^{1/2}$ (fm)	5.45	5.43	3.44	3.37
$\langle r^2\rangle_{n}^{1/2}$ (fm)	6.06	5.71	3.41	—
$\langle r^2\rangle^{1/2}$ (fm)	5.83	—	3.43	—
$r_n - r_p$ (fm)	0.61	0.28	−0.03	—
$\rho(0)$ (fm^{-3})	0.143	≈0.16	0.201	≈0.17
$\varepsilon_F^{(n)}$ (MeV)	−7.54	−7.37	−15.64	−15.64
$\varepsilon_F^{(p)}$ (MeV)	−7.94	−8.00	−6.60	−8.33

IV. RESULTS AND DISCUSSION

A. Ground-state properties of the isolated nuclei

The quality of the unperturbed mean field determines the reliability of the calculated polarization, and therefore the ground-state properties of the two nuclei have been examined first. The results are collected in Table I, and the density profiles and single-particle levels are shown in Fig. 4.

The integrated particle numbers reproduce the input values to better than 0.1%. The radii have to be compared with the corresponding measured quantity: what is measured in electron scattering is the charge radius, whereas what the calculation delivers directly is the point-nucleon distribution. Folding the calculated point-proton distribution with the proton charge form factor gives a charge radius of 5.52 fm for ^{208}Pb against the measured 5.501 fm [22]; that is, agreement to 0.4%, and 3.55 fm for ^{40}Ca against 3.478 fm, high by 2.2%. The proton distributions are therefore well reproduced.

The neutron distributions are not reproduced as well. The calculated neutron skin of ^{208}Pb, $r_n - r_p = 0.61$ fm, is more than twice the measured 0.283 ± 0.071 fm [25]. This is a known feature of the Woods–Saxon parametrization used here, in which the neutron and proton central radii are independent parameters, $r_0 = 1.347$ and 1.275 fm, so that the isovector geometry is not constrained by any observable. It accounts for the two remaining discrepancies of Table I. The matter radius of ^{208}Pb exceeds the charge radius not because the nucleus is too large but because the neutrons lie too far out, and the central density of 0.143 fm^{-3} falls below saturation for the same reason, the neutron central density being 0.067 fm^{-3} against the 0.097 fm^{-3} which a common proton and neutron shape would give. The apparent central depression of ^{208}Pb is therefore a property of the parametrization and should not be identified with the shallow depression of the measured charge distribution [23]. For ^{40}Ca, with $N = Z$, the skin vanishes, and the central density of 0.201 fm^{-3} reflects the genuine central bump of a light $N = Z$ nucleus, enhanced in a mean field in which the short-range correlations are absent.

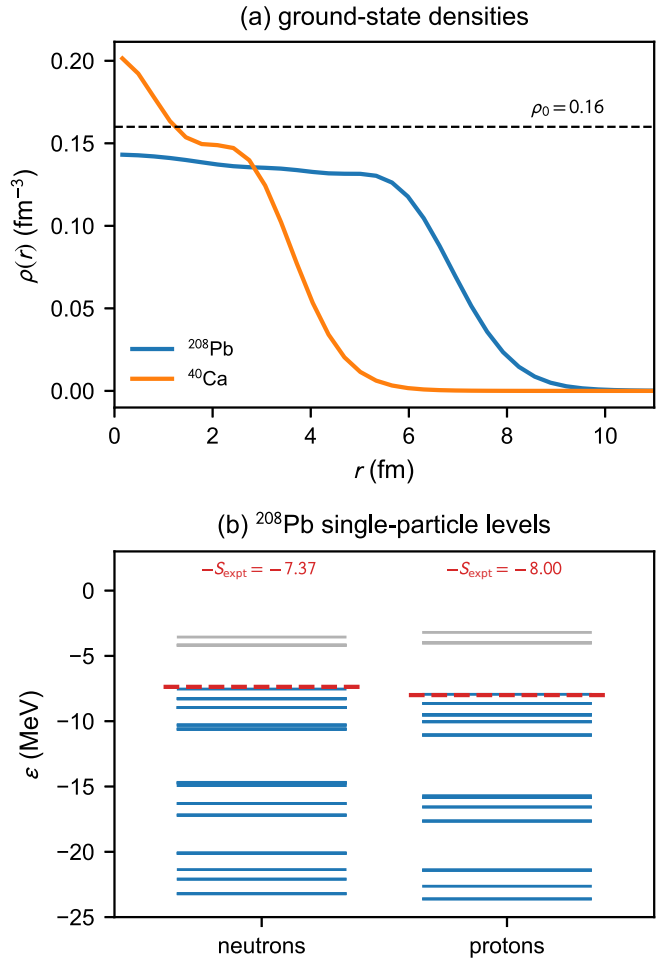


FIG. 4. (a) Radial density distributions of the isolated ^{208}Pb and ^{40}Ca nuclei obtained in the present calculation. The dashed line indicates the saturation density. (b) Single-particle levels of ^{208}Pb near the Fermi surface; occupied levels are shown by full lines and the lowest empty ones by gray lines. The dashed lines give the experimental neutron and proton separation energies with the opposite sign.

The consequence for the present work is limited. The polarization is driven by the Coulomb field, which acts on the protons, and the proton distribution is the one which is well reproduced, so that the dipole and quadrupole responses are not directly affected. The nuclear part of the external field is, however, sampled in the surface region where the excess neutrons are located, so that the nuclear contribution to ΔQ_{20} and the validity limit of Sec. III inherit this uncertainty; its size is examined in Sec. IV F.

The last occupied single-particle level is to be compared with the one-nucleon separation energy taken with the opposite sign, $\varepsilon_F = -S$. For ^{208}Pb the last occupied neutron level lies at −7.54 MeV against $-S_n = -7.368$ MeV [24], and the corresponding proton level at −7.94 MeV against

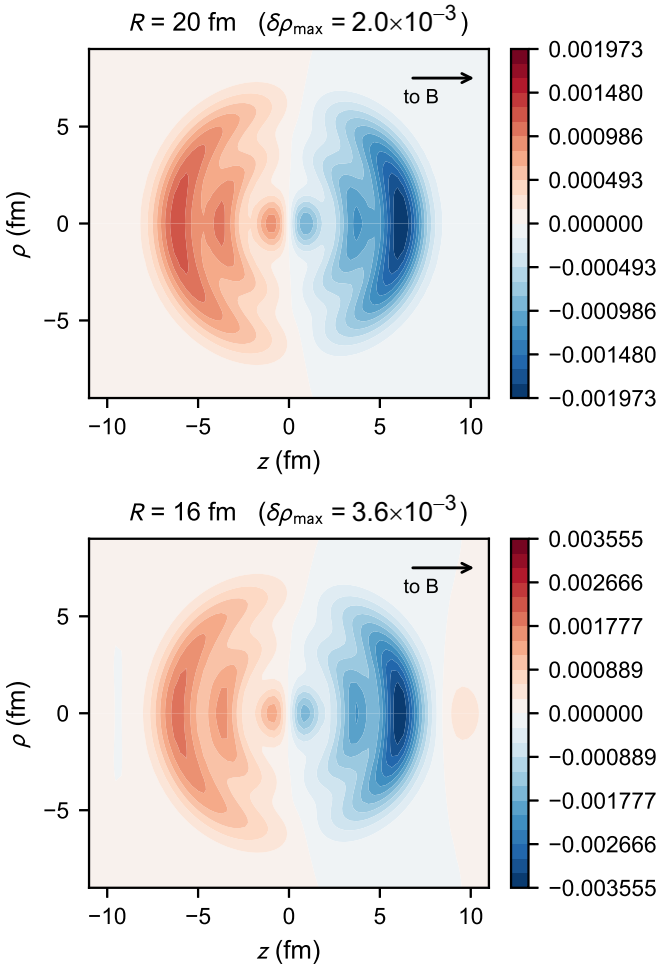


FIG. 5. Density change $\delta\rho(z, \rho)$ induced in ^{208}Pb by the presence of ^{40}Ca at $R = 20$ fm (upper panel) and $R = 16$ fm (lower panel). The partner nucleus is located on the positive z axis, as indicated by the arrow. Red and blue correspond to an increase and to a decrease in density, respectively.

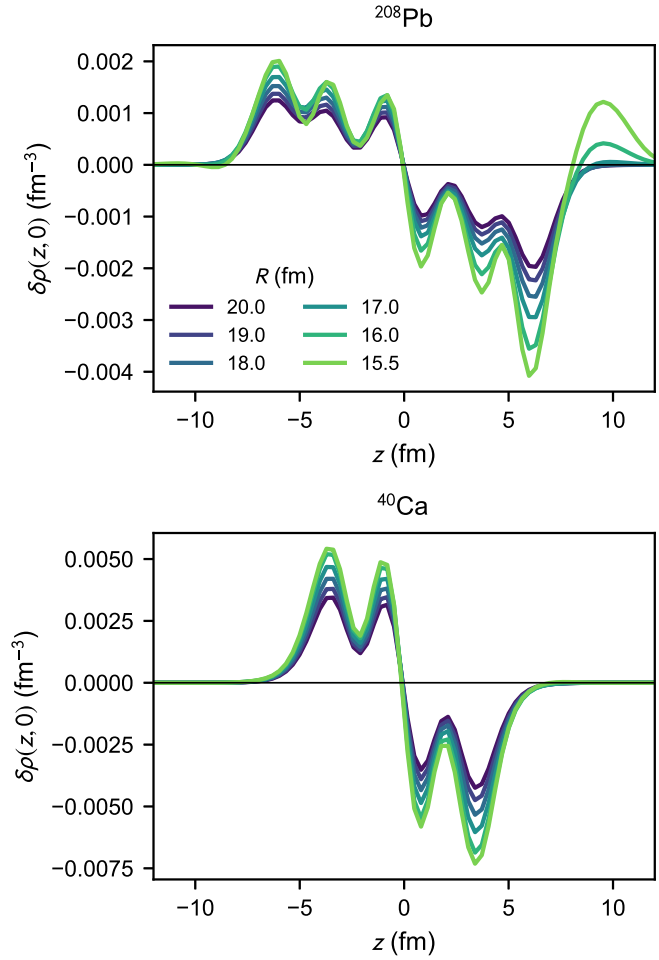


FIG. 6. Density change along the symmetry axis for ^{208}Pb (upper panel) and ^{40}Ca (lower panel) at the separations indicated. The partner nucleus is on the positive-z side.

$-S_p = -8.004$ MeV. For ^{40}Ca the neutron Fermi energy of -15.64 MeV reproduces $-S_n = -15.641$ MeV exactly, while the proton level at -6.60 MeV lies about 1.7 MeV above $-S_p = -8.328$ MeV; that is, it is less bound than the measured value. This deviation of the Rost parametrization for the lighter partner has been kept in mind in the interpretation of the results for ^{40}Ca.

B. Structure of the polarization density

The density change induced in ^{208}Pb by ^{40}Ca is shown in Fig. 5 for two separations. The polarization is concentrated in the surface region of the nucleus. At $R = 16$ fm, the fraction of $|\delta\rho|$ contained between $r = 4$ and $r = 9$ fm amounts to about 88% of the total, and the weighted mean radius of $|\delta\rho|$ is 6.0 fm, close to the root-mean-square radius of the nucleus itself. The interior of the nucleus is almost unaffected, which is a consequence of the fact that the external field is smooth over the nuclear volume and that the deeply bound orbitals are separated from the empty ones by a large energy denominator.

The pattern of Fig. 5 shows an accumulation of density on the side opposite to the partner and a depletion on the side facing it. This is the expected response of a positively charged system to the repulsive field of another positive charge. The effect is essentially a displacement of the proton distribution: the calculated dipole moment of the total density change at $R = 20$ fm is $\Delta D_1 = -4.26$ fm, and the value obtained from the protons alone is -4.26 fm, so that the neutrons do not contribute. The corresponding shift of the center of the proton distribution with respect to the center of the mean field is $\Delta D_1/Z = -0.052$ fm. It should be noted that the mean field of the nucleus A is held fixed at the origin in the present treatment, so that this dipole moment describes the displacement of the charge distribution relative to the mean-field center and should not be identified with an intrinsic $E1$ moment of a freely recoiling nucleus.

The behavior of $\delta\rho$ along the symmetry axis is presented in Fig. 6 for both partners and for all separations considered. The amplitude of the polarization grows monotonically as the two nuclei approach, and the shape of the curves changes little, which indicates that the response remains dominated by the same few particle-hole configurations over the whole range.

TABLE II. Induced quadrupole moment, mean-square radius change, dipole moment, and polarization energy of ^{208}Pb and ^{40}Ca as functions of the center-to-center distance. ΔQ_{20} is referred to the center of mass (c.m.) of the total density, Eq. (26). ΔD_1 is the moment about the fixed center of the mean field and ΔD_1^{E1} the translationally invariant combination of Eq. (29). ΔE is the polarization energy of Eq. (24). The last column gives the number of nucleons which appear beyond $z_s = 10$ fm and serves as a measure of the reliability of the one-center description.

R (fm)	$\Delta Q_{20}^{\text{c.m.}}$ (fm^2)	$\Delta\langle r^2\rangle$ (fm^2)	ΔD_1 (fm)	ΔD_1^{E1} (fm)	ΔE (MeV)	ΔN_{leak}
			^{208}Pb			
20.0	−7.00	0.0009	−4.26	−2.58	−0.160	$<10^{-3}$
19.0	−8.13	0.0011	−4.72	−2.86	−0.197	$<10^{-3}$
18.0	−9.44	0.0016	−5.24	−3.18	−0.246	$<10^{-3}$
17.0	−10.65	0.0030	−5.83	−3.58	−0.313	0.001
16.0	−9.79	0.0098	−6.34	−4.12	−0.430	0.008
15.5	−4.85	0.0230	−6.30	−4.55	−0.610	0.023
			^{40}Ca			
20.0	−1.04	0.0102	−2.21	−1.10	−0.329	$<10^{-3}$
19.0	−1.19	0.0125	−2.44	−1.22	−0.404	$<10^{-3}$
18.0	−1.35	0.0155	−2.72	−1.36	−0.500	$<10^{-3}$
17.0	−1.54	0.0196	−3.03	−1.52	−0.626	$<10^{-3}$
16.0	−1.65	0.0264	−3.39	−1.71	−0.792	0.001
15.5	−1.55	0.0325	−3.57	−1.82	−0.894	0.002

C. Quadrupole polarization

The induced quadrupole moments are given in Table II and shown in Fig. 7 together with the linear-response results and their decomposition into the Coulomb and nuclear contributions. The induced quadrupole moment is negative for both partners over the whole range of separations; that is, the density is compressed along the internuclear axis, and the resulting shape is oblate. This may appear surprising at first sight, since the nuclear attraction of the partner acts in the direction of an elongation, but the decomposition shown in Fig. 7 makes the origin of the effect clear. The quadrupole component of the Coulomb field, Eq. (10), raises the potential at the poles of the nucleus relative to its equator, so that the protons are pushed toward the equatorial plane. A repulsive tidal field compresses, whereas an attractive one, such as the gravitational tide, elongates. The nuclear contribution is indeed positive, but it is much smaller in the region where the calculation is valid.

The relative importance of the two contributions changes rapidly with the separation. At $R = 20$ fm the nuclear part of ΔQ_{20} amounts to 0.004 fm^2 against −7.25 fm^2 from the Coulomb part; that is, to less than 0.1%. At $R = 17$ fm it has grown to 0.60 fm^2, and at $R = 15.5$ fm it reaches 5.29 fm^2, about a third of the Coulomb value. This rapid growth is a direct consequence of the zero range of the Migdal force: the external nuclear field is significant only where the density of the partner is significant, and the overlap of the tail of ^{208}Pb with the surface of ^{40}Ca grows very fast once the two surfaces approach each other.

It should be stressed that the oblate character found here is a property of the range of separations in which the Coulomb tidal field dominates. The nuclear contribution grows exponentially as the surfaces approach, with an e-folding length of 0.62 fm obtained from the present results, which is close to the diffuseness of the density distributions. An extrapolation of this behavior together with the R^{-3} Coulomb term indicates a change of sign near $R \simeq 15$ fm; that is, just below the range accessible to the present calculation. Since the Coulomb barrier of the ^{40}Ca + ^{208}Pb system is located near $R \simeq 13$ fm, a prolate polarization is to be expected in the barrier region itself, in agreement with the elongation reported in dynamical models of fusion. The two pictures correspond to different ranges of the separation rather than to a disagreement.

The competition of the two contributions produces a turnover in the magnitude of the polarization. For ^{208}Pb the modulus of $\Delta Q_{20}^{\text{c.m.}}$ increases from 7.00 fm^2 at $R = 20$ fm to 10.65 fm^2 at $R = 17$ fm and then decreases again to 4.85 fm^2 at $R = 15.5$ fm, the maximum being reached at $R \simeq 17$ fm. For ^{40}Ca the same behavior is observed, with the maximum at $R \simeq 16$ fm. It is important to note that no change of sign takes place within the range of separations where the one-center description is valid; the cancellation between the Coulomb and nuclear tidal fields remains partial down to $R = 15.5$ fm.

The Coulomb part of the response provides a test of the calculations. According to Eq. (10), the quadrupole driving term scales as R^{-3}, and if the response is linear, the induced moment must follow the same law. Figure 8 shows that the calculated Coulomb contribution reproduces the R^{-3} dependence for both nuclei over the whole range, with deviations below the thickness of the line.

D. Induced deformation parameter

It is convenient to express the induced quadrupole moment through the dimensionless deformation parameter, defined in the usual way as

$$\beta_2 = \frac{4\pi}{3AR_0^2}\int \rho(\boldsymbol{r}) r^2 Y_{20}(\theta) d^3r, \quad R_0 = 1.2A^{1/3}, \tag{32}$$

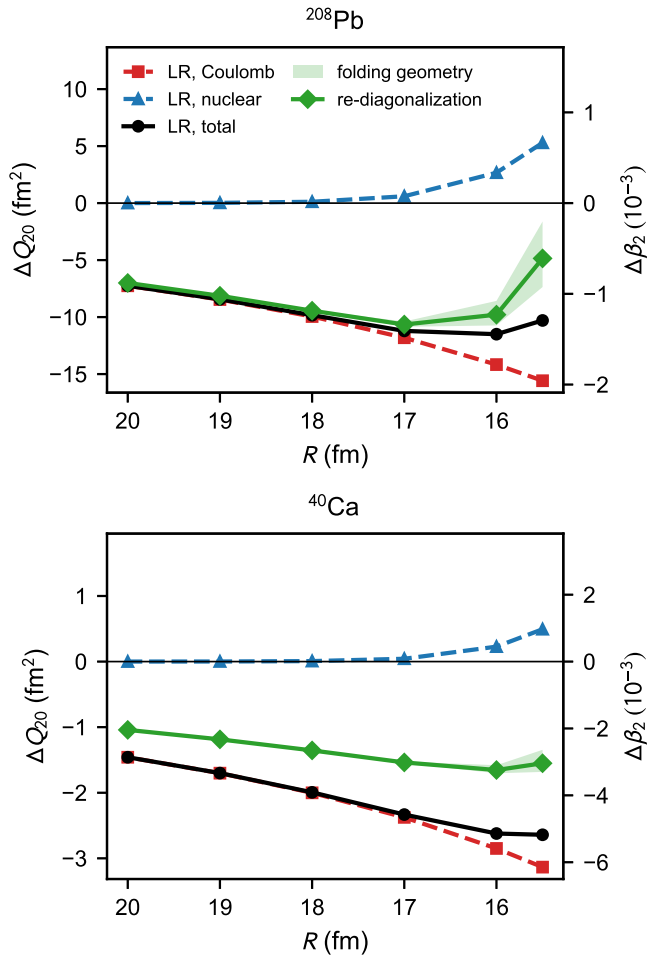


FIG. 7. Induced quadrupole moment of ^{208}Pb (upper panel) and ^{40}Ca (lower panel) as a function of the center-to-center distance, referred to the center of mass of the total density, Eq. (26). The full symbols connected by the solid green line show the result of the rediagonalization and the shaded band the spread produced by varying the diffuseness and the radii of the folding densities as in Table IV; the black line is the total linear-response result. The dashed red and blue lines give the Coulomb and nuclear contributions to the linear-response value separately. The right-hand scale gives the corresponding induced quadrupole deformation parameter of Eq. (33).

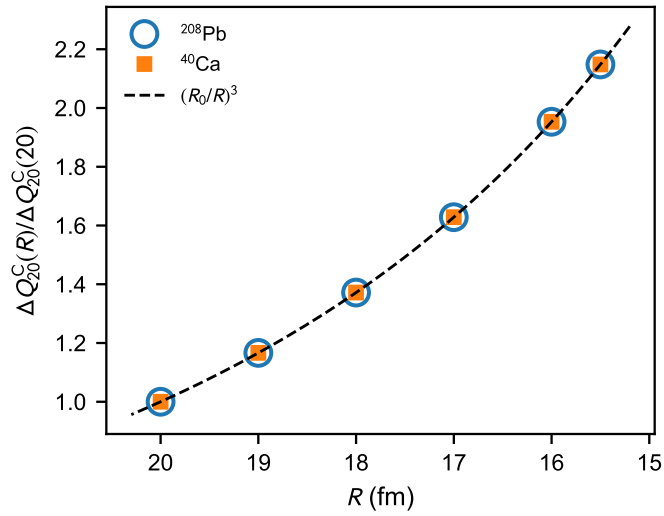


FIG. 8. Coulomb contribution to the induced quadrupole moment, normalized to its value at $R = 20$ fm, in comparison with the R^{-3} dependence expected for a tidal field. The results for the two nuclei coincide, and ^{208}Pb is therefore drawn with an open symbol.

which is the convention in which the tabulated ground-state deformations are given [26,27]. With the operators used here, $2z^2 - \rho_\perp^2$ for the quadrupole and P_3 of Eq. (28) for the octupole, the changes induced by the partner are

$$\Delta\beta_2 = \frac{\sqrt{5\pi}\,\Delta Q_{20}^{\text{c.m.}}}{3AR_0^2}, \quad \Delta\beta_3 = \frac{2\sqrt{7\pi}\,\Delta Q_{30}^{\text{c.m.}}}{3AR_0^3}, \tag{33}$$

evaluated with the recentered moments of Eq. (26) and the octupole of Sec. II F. The values obtained in the two treatments are given in Table III.

The induced deformations are small, of the order of 10^{-3}, which justifies *a posteriori* the treatment of the polarization as a perturbation of the ground state. It is important to note that although the induced quadrupole moment of ^{208}Pb is about seven times larger than that of ^{40}Ca in absolute value, the deformation parameter behaves in the opposite way: $\Delta\beta_2$ of the light partner is between two and three times that of the heavy one at every separation. The reason is the normalization by AR_0^2 in Eq. (32), which is about sixteen times smaller

TABLE III. Induced quadrupole and octupole deformation parameters (in units of 10^{-3}) of the two partners. $\Delta\beta_2$ and $\Delta\beta_3$ are obtained from the moments referred to the center of mass of the total density, Eq. (26); RD denotes rediagonalization and LR first-order perturbation theory. The last column of each block gives the ratio of the rediagonalized to the first-order quadrupole moment evaluated in the shape frame of Eq. (26), which is the frame in which the two treatments describe the same quantity. Values below $R \simeq 15.5$ fm are affected by the transfer of amplitude to the partner and are shown for completeness only.

	^{208}Pb				^{40}Ca			
R (fm)	$\Delta\beta_2^{\text{RD}}$	$\Delta\beta_2^{\text{LR}}$	$\Delta\beta_3^{\text{RD}}$	Ratio	$\Delta\beta_2^{\text{RD}}$	$\Delta\beta_2^{\text{LR}}$	$\Delta\beta_3^{\text{RD}}$	Ratio
20.0	−0.880	−0.911	−0.349	1.003	−2.043	−2.860	−0.939	0.882
19.0	−1.022	−1.060	−0.423	1.002	−2.326	−3.334	−1.130	0.873
18.0	−1.186	−1.235	−0.501	1.002	−2.656	−3.910	−1.360	0.864
17.0	−1.338	−1.409	−0.506	0.996	−3.016	−4.574	−1.583	0.857
16.0	−1.230	−1.445	0.082	0.910	−3.243	−5.141	−1.438	0.854
15.5	−0.609	−1.293	1.583	0.552	−3.040	−5.179	−0.645	0.838

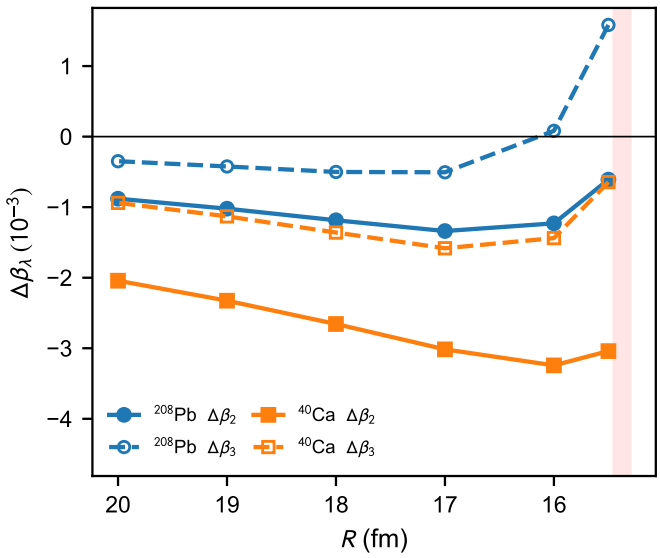


FIG. 9. Induced quadrupole (full symbols, solid lines) and octupole (open symbols, dashed lines) deformation parameters of the two partners as functions of the center-to-center distance, both referred to the center of mass of the total density. The shaded band marks the limit of validity established in Sec. III. The change of sign of $\Delta\beta_3$ for ^{208}Pb near $R \simeq 16.1$ fm is produced by the transfer of amplitude toward the partner and is an early indicator of the breakdown of the one-center description.

for ^{40}Ca. The lighter nucleus is therefore the more strongly polarized of the two in relative terms, both because it is softer and because the field of ^{208}Pb is four times stronger than the field of ^{40}Ca. This is relevant for the DNS description, in which the deformation parameters of the two fragments enter the driving potential on an equal footing.

The induced octupole moment is given in the same table and is not negligible in relative terms. In the range $R \geqslant 17$ fm, the ratio $|\Delta\beta_3/\Delta\beta_2|$ is close to 0.4 for ^{208}Pb and to 0.5 for ^{40}Ca. At $R = 20$ fm the values are -0.35 against -0.88 in units of 10^{-3} for ^{208}Pb, and -0.94 against -2.04 for ^{40}Ca. This is the multipole content of the forward-backward asymmetry, which is visible in Fig. 5 but is not quantified by the density maps. Since the partner is located on one side of the nucleus, the external field is not invariant under $z \to -z$, and all the odd multipoles of $\delta\rho$ are allowed. Both $\Delta\beta_2$ and $\Delta\beta_3$ are shown as functions of the separation in Fig. 9. Being an odd moment, $\Delta\beta_3$ vanishes identically for the isolated nucleus, and the value -0.000 obtained for spherical ^{208}Pb is a check of the treatment of the two (Λ, σ) channels in Eq. (19), which have to be combined incoherently: summing them coherently leaves the even multipoles untouched but makes the odd ones spurious.

The octupole is also the more sensitive of the two moments to the breakdown of the one-center picture, and it provides a third diagnostic of it. For ^{208}Pb it grows steadily from -0.35 to -0.51 in units of 10^{-3} between $R = 20$ and 17 fm, then changes sign and reaches $+1.58$ at $R = 15.5$ fm, a value which is larger than the quadrupole one itself. The amplitude transferred to the region of the partner is located at large positive z and contributes to an odd moment with the third power of the lever arm, so that $\Delta\beta_3$ responds to the leakage far more sharply than $\Delta\beta_2$ does. Its change of sign near $R \simeq 16.1$ fm is a warning that the description is deteriorating, and it occurs at a separation at which the quadrupole moment is still smooth.

E. Comparison with the linear-response treatment

The comparison of the two treatments is meaningful only in a frame in which they describe the same quantity. As shown in Sec. II F, the kinematic term $2N_q d^2$ is of second order in $U_{\rm ext}$ and is absent from the first-order expression by construction, while the rediagonalization contains it. It is not a small correction in the present case: at $R = 20$ fm it amounts to 0.44 fm^2 for ^{208}Pb and to 0.49 fm^2 for ^{40}Ca, against laboratory-frame differences between the two treatments of 0.42 and 0.66 fm^2. The apparent discrepancy is thus almost entirely kinematic for the heavy partner and about three-quarters kinematic for the light one. The comparison is therefore made in the shape frame, and the laboratory-frame ratio is retained as the dotted curve of Fig. 10(a).

In that frame, the response of ^{208}Pb is linear. The ratio of the rediagonalized moment to the first-order one is 1.003, 1.002, 1.002, and 0.996 at $R = 20$, 19, 18, and 17 fm. The individual moments are basis dependent at the 2% level over $N_{\rm max} = 10$ to 15, but their ratio is not, since the leading error is common to two treatments built from the same basis; both sides have been recomputed at $N_{\rm max} = 10$, 12, and 15 in order to establish this, as reported in Sec. IV F. No higher-order contribution to the quadrupole response of the heavy partner is resolvable at these separations. Below $R = 17$ fm the ratio falls to 0.910 and 0.552, which is the onset of the breakdown documented in Sec. III and not a nonlinearity, since it coincides with the rise of $\Delta N_{\rm leak}$ and with the change of sign of the octupole moment.

For ^{40}Ca a genuine nonlinearity survives, but it is much smaller than the laboratory-frame comparison suggested. The ratio is 0.882 at $R = 20$ fm and varies slowly to 0.838 at $R = 15.5$ fm, so that the terms beyond the first order contribute 12% to 16% and not the 45% obtained without the kinematic correction. This figure is not fully converged with the basis, as Sec. IV F shows, so that the departure from unity is established, but its magnitude is a lower estimate. Its origin is the expected one: the charge of ^{208}Pb is four times that of ^{40}Ca, so that the field acting on the lighter partner is stronger, and the lighter nucleus has the softer surface.

The residue is a property of the response and not a further artifact, as the dependence on the strength of the field shows. Figure 10(b) gives the ratio, again in the shape frame, as the switching parameter λ of Eq. (16) is varied from 0.1 to 1 at $R = 20$ fm with the Coulomb field alone. For ^{208}Pb it stays between 0.995 and 1.003 over the whole range, while for ^{40}Ca it decreases smoothly from 0.986 to 0.882, extrapolating to unity as $\lambda \to 0$ as it must. The scan has been made at a single separation and with the Coulomb field only, so that it tests the dependence on the strength of the field and not the dependence on the separation, which is the subject of Fig. 10(a). The agreement of the two implementations in the weak-field limit is a consistency check of both.

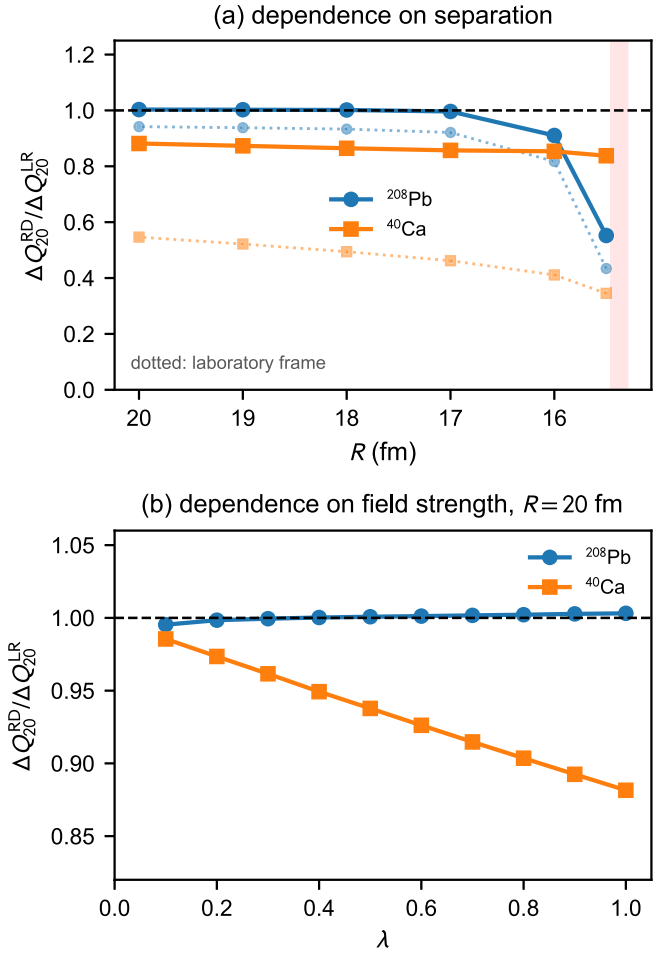


FIG. 10. Ratio of the induced quadrupole moment obtained by rediagonalization to its first-order value, both evaluated in the shape frame of Eq. (26). (a) As a function of the center-to-center distance at full strength of the external field; the dotted curves give the same ratio in the laboratory frame, whose departure from unity is the kinematic $2N_q d^2$ term rather than a nonlinear response, and the shaded band marks the limit of validity of Sec. III. (b) As a function of the switching parameter λ of Eq. (16) at $R = 20$ fm for the Coulomb field alone.

F. Sensitivity to the geometry of the folding densities

The diffuseness $a_0 = 0.54$ fm and the radius coefficients of Eq. (15) are taken over from the DNS driving code and are not constrained by any observable of the present calculation; the mean field, moreover, uses the independent Woods–Saxon geometry of Sec. IIA and not the same prescription. Because the Migdal force is of zero range, the external nuclear field follows ρ_B directly and is exponentially sensitive to both parameters, so that the size of the resulting uncertainty has to be established and not assumed. The calculation has therefore been repeated with $a_0 = 0.50$ and 0.58 fm and with both radius coefficients scaled by 0.97 and 1.03, which spans the range over which such parametrizations differ in the literature. It should be stressed that this scan varies the densities entering the folded field of the partner and nothing else. The isovector geometry of the Woods–Saxon mean field of the nucleus under study, which gives a neutron skin more than twice the measured one, as shown in Sec. IV A, is a separate source of the model uncertainty and is not probed here.

TABLE IV. Induced quadrupole deformation $\Delta\beta_2$ (in units of 10^{-3}, referred to the center of mass) for the five geometries of the folding densities, and the total spread relative to the baseline value.

R (fm)	Base	$a_0 = 0.50$	$a_0 = 0.58$	$0.97R_i$	$1.03R_i$	Spread
			^{208}Pb			
20.0	−0.880	−0.880	−0.880	−0.880	−0.880	0.1%
18.0	−1.186	−1.192	−1.178	−1.189	−1.183	1.1%
17.0	−1.339	−1.363	−1.306	−1.354	−1.321	4.3%
16.0	−1.230	−1.349	−1.078	−1.323	−1.112	22%
15.5	−0.610	−0.925	−0.203	−0.896	−0.215	119%
			^{40}Ca			
20.0	−2.044	−2.044	−2.044	−2.044	−2.044	0.0%
18.0	−2.658	−2.662	−2.652	−2.660	−2.654	0.4%
17.0	−3.018	−3.037	−2.991	−3.033	−2.995	1.5%
16.0	−3.245	−3.336	−3.128	−3.342	−3.101	7.4%
15.5	−3.042	−3.249	−2.784	−3.301	−2.641	22%

The results are collected in Table IV and the corresponding band is shown in Fig. 7. The structure of the uncertainty follows directly from the decomposition of the response. Where the Coulomb tidal field dominates, the induced moment does not depend on the folding geometry at all: the spread is below 0.1% at $R = 20$ fm and about 1% at $R = 18$ fm for both partners. It grows to 4.3% for ^{208}Pb and to 1.5% for ^{40}Ca at $R = 17$ fm, and to 22% and 7.4% at $R = 16$ fm. At $R = 15.5$ fm the value for ^{208}Pb ranges from −0.93 to −0.20 in units of 10^{-3}, that is, by a factor of 4.5, while for ^{40}Ca the spread is 22%. The quantities quoted in this work are therefore firm over most of the range and become geometry dominated only in the last fermi before the one-center description fails, where they are in any case no longer reliable for the reason given in Sec. III.

A second numerical uncertainty concerns the comparison of the two treatments rather than the external field. The individual moments are basis dependent at the 2% level over $N_{\max} = 10$ to 15, and the ratio used in Sec. IV E need not inherit that dependence, since the two treatments are built from the same basis and the leading error is common to them. Recomputing both sides at $N_{\max} = 10$, 12, and 15 gives, for $\Delta Q_{20}^{\mathrm{sh,RD}}/\Delta Q_{20}^{\mathrm{sh,LR}}$, the following results:

	R (fm)	10	12	15	Spread
^{208}Pb	20.0	1.0047	1.0044	1.0031	0.2%
	17.0	1.0026	1.0022	0.9963	0.6%
^{40}Ca	20.0	0.9261	0.9026	0.8816	5.0%
	17.0	0.9057	0.8791	0.8570	5.7%

The cancellation is effective for ^{208}Pb: the ratio moves by 0.2% and 0.6%, where the moments themselves move by 2%.

TABLE V. Polarization energy of the ^{40}Ca + ^{208}Pb system, $|\Delta V| = |\Delta E_A + \Delta E_B|$ in MeV. The second column is the energy as computed, obtained from the coupling-constant integral of Eq. (35) at every separation. The third is the corrected value, in which the Coulomb dipole component alone is rescaled by $\alpha_D^{\rm expt}/\alpha_D$, the quadrupole and the nuclear contributions being left unchanged; the fourth is its uncertainty, from the experimental error on α_D and from the ambiguity of the translational prescription. The last column is the classical estimate of Eq. (37), which covers the Coulomb dipole channel only and is therefore expected to fall below the corrected value once the nuclear contribution becomes appreciable. The radial force implied by these energies is shown in Fig. 11.

R (fm)	Computed	Corrected	Range	Eq. (37)
20.0	0.491	0.105	0.096–0.114	0.094
19.0	0.604	0.131	0.120–0.142	0.116
18.0	0.751	0.165	0.151–0.179	0.144
17.0	0.946	0.213	0.196–0.230	0.181
16.0	1.225	0.307	0.286–0.329	0.230
15.5	1.463	0.450	0.427–0.474	0.261

Its distance from unity, 0.3% and 0.4%, is of the same size as that residual dependence, so that the proper statement is that no higher-order contribution is resolvable and not that it vanishes. For ^{40}Ca the cancellation is much less complete and the ratio has not converged: it falls monotonically by about 5% between $N_{\rm max} = 10$ and 15 and is still moving at the largest basis available, the successive changes being -0.024 and -0.021. The departure from unity is therefore established, being far larger than the drift, but its magnitude is a lower estimate. Values of $N_{\rm max}$ above 15 are not accessible in the present implementation.

Two conclusions of the preceding sections should be examined against this band. The position of the turnover is stable at the resolution of the present grid: the modulus of $\Delta\beta_2$ peaks at the same sampled separation, $R = 17$ fm for ^{208}Pb and $R = 16$ fm for ^{40}Ca, in every one of the five geometries. Since the separations are spaced by 1 fm, this establishes that the turnover does not move by a grid step and not that its position is unchanged, for which a finer grid would be needed. The extrapolated change of sign is not stable in the same sense: repeating the extrapolation of Sec. IV C for each geometry places it between 14.4 and 15.4 fm, so that the value $R \simeq 15$ fm quoted there carries an uncertainty of at least ± 0.5 fm from this source alone, in addition to the fact that it lies below the limit of validity of the calculation. The statement that a prolate polarization is to be expected in the barrier region is a qualitative one and should be read as such.

G. Polarization energy and radius change

The polarization energy of Eq. (24) and the change of the mean-square radius are given in Tables II and V. The polarization energy is negative for both partners, as it must be for an induced response, and it grows in magnitude as the separation decreases. At $R = 15.5$ fm it amounts to -0.61 MeV for ^{208}Pb and to -0.89 MeV for ^{40}Ca; the coupling-constant integration of Eq. (35) below gives -0.56 and -0.90 MeV for the same configurations, and the sum of the two partners is -1.46 MeV against -1.50 MeV from the second-order expression.

It is important to note that this energy is not a measure of the quadrupole polarization, which is the subject of the preceding sections. Inserting the multipole expansion of Eq. (10) into Eq. (24) gives

$$\Delta E \simeq \frac{Z_B e^2}{2R^2}\Delta D_1 + \frac{Z_B e^2}{2R^3}\frac{\Delta Q_{20}}{2}, \tag{34}$$

and the two terms reproduce the calculated values to better than 2% at $R \geqslant 18$ fm. The first term accounts for 95% to 96% of ΔE for ^{208}Pb and for 99% for ^{40}Ca. The polarization energy is therefore a dipole quantity, and the quadrupole deformation discussed above contributes only a few percent of it.

Equation (24) carries the factor of $1/2$ of the second-order perturbation theory, which is exact only if the response is linear in the external field. Since the quadrupole response of ^{40}Ca is not linear, the polarization energy has been checked by the coupling-constant integration. With $\hat{h} = \hat{h}_0 + \lambda U_{\rm ext}$ the Hellmann–Feynman theorem gives $dE/d\lambda = \langle U_{\rm ext}\rangle_\lambda$, so that

$$\Delta E = \int_0^1 d\lambda \int U_{\rm ext}\delta\rho_\lambda d^3r, \tag{35}$$

which reduces to Eq. (24) only when $\delta\rho_\lambda = \lambda\delta\rho_1$. The integral has been evaluated by the trapezoidal rule on a uniform grid of eleven points, $\lambda = 0, 0.1, \ldots, 1$, the value at $\lambda = 0$ being exactly zero. The quadrature is converged. Halving the number of intervals changes the result by less than 2.5×10^{-4} MeV at every separation except for ^{208}Pb at $R = 15.5$ fm, where the change is 1.8×10^{-3} MeV, and Simpson's rule on the same grid agrees with the trapezoidal value to 6×10^{-4} MeV or better.

The integration has been carried out for both partners at all six separations. The second-order expression of Eq. (24) reproduces the result to better than 1% in eleven of the twelve cases, the deviations lying between -0.99% and $+0.99\%$. The exception is ^{208}Pb at $R = 15.5$ fm, where it exceeds the coupling-constant value by 0.05 MeV, or 9%. The factor of $1/2$ is therefore adequate over the range in which the one-center description holds, and it is the coupling-constant values which have been used for Table V. It should be noted that this is a statement about the energy and not about the density response: a density response which is linear in the field already gives an energy quadratic in it, and what the test establishes is that the energy is well approximated by its second-order expression and not that the response is linear. That this holds for ^{40}Ca while its quadrupole moment is visibly nonlinear is consistent with the decomposition given above, since ΔE is carried by the dipole channel and the nonlinear quadrupole channel contributes only a few percent of it.

The dipole response obtained here is not screened, since the residual particle-hole interaction is not included in Eq. (16). Its size can be tested against the measured static dipole polarizability, which is the one quantity of the present calculation for which direct experimental data exist. Evaluating

$$\alpha_D = 2ge^2\sum_{ph}\frac{|\langle p|\hat{D}_z|h\rangle|^2}{\varepsilon_p - \varepsilon_h}, \quad \hat{D}_z = \sum_i q_i z_i, \tag{36}$$

where z_i is measured in fm, q_i is the charge of nucleon i in units of e, and $e^2 = 1.44$ MeV fm, so that α_D has the dimension fm^3. Evaluating it for the isolated nuclei, with the dipole operator taken with the full proton charge, $q_p = 1$ and $q_n = 0$, gives 85.7 fm^3 for ^{208}Pb and 10.9 fm^3 for ^{40}Ca. These values agree with those extracted from ΔD_1 and the uniform part of the external field, 85 and 11 fm^3, which are moreover almost independent of R; the two determinations are independent, and their agreement confirms the linearity of the response.

Part of this response is spurious. A uniform field acting on the protons of a nucleus whose mean field is anchored at the origin displaces the whole system against an artificial restoring force, and this center-of-mass motion is not a polarization. It is removed in the standard way by using the effective charges $q_p = N/A$ and $q_n = -Z/A$ in Eq. (36), which gives 57.3 fm^3 for ^{208}Pb and 5.26 fm^3 for ^{40}Ca. The remaining values exceed the measured 20.1 ± 0.6 fm^3 [28] and 1.92 ± 0.17 fm^3 [29] by factors of 2.9 and 2.7, respectively. It is important to note that these two factors are equal within the accuracy of the comparison, although the two nuclei differ by a factor of 5 in mass. The overestimate is therefore a systematic property of the unperturbed particle-hole response and not a numerical deficiency: the isovector restoring force which shifts the dipole strength up into the giant resonance is absent, and it is known to reduce the inverse energy-weighted sum rule by a factor of this order.

Two corrections to ΔE follow from this, and neither of them is small. Both are phenomenological rescalings of the computed energy and not recalculations of it: in the anchored independent-particle model the response has been generated by the proton-only Coulomb field, and that field is not altered by evaluating a different operator on the resulting $\delta\rho$.

They apply, moreover, to the Coulomb dipole part alone. The multipole expansion of Eq. (34) separates ΔE into that part, the quadrupole term and a remainder which carries the nuclear field and the higher multipoles. The dipole fraction is 96% for ^{208}Pb at $R = 20$ fm, but it falls to 93% at 17 fm, 83% at 16 fm and 62% at 15.5 fm as the short-ranged nuclear field switches on, while for ^{40}Ca it stays between 99% and 98%. Rescaling the whole of ΔE would suppress the nuclear contribution as though it were an unscreened $E1$ response, which at the smallest separations it is not, and therefore only the dipole term is rescaled below. The isoscalar quadrupole response in particular carries no screening of this kind and is, if anything, underestimated here, the residual interaction in that channel being attractive.

The rescaling factor telescopes: the removal of the translational component multiplies the dipole term by $\alpha_D^{\rm eff}/\alpha_D$, and the screening multiplies it by $\alpha_D^{\rm expt}/\alpha_D^{\rm eff}$, so that the product is $\alpha_D^{\rm expt}/\alpha_D$, equal to 0.235 for ^{208}Pb and to 0.176 for ^{40}Ca. The intermediate effective-charge polarizability cancels, which removes one ambiguity. The alternative prescription for the translational step, in which only the measured operator is changed, and the factor is N/A, differs by 9% for ^{208}Pb and by 3% for ^{40}Ca and is carried through as an uncertainty.

With the rescaling applied in this way, and with the coupling-constant integral of Eq. (35) taken as the base energy at every separation, the polarization energy of the system is 0.105 MeV at $R = 20$ fm and 0.450 MeV at $R = 15.5$ fm, against 0.491 and 1.463 MeV as computed. Table V gives all six separations together with an uncertainty obtained from the experimental errors on α_D, 20.1 ± 0.6 fm^3 [28] and 1.92 ± 0.17 fm^3 [29], and from the ambiguity described above. This uncertainty falls from 8.6% of the energy at the largest separation to 5.2% at the smallest one.

An independent estimate is available for the dominant channel. The classical adiabatic dipole polarization potential of two mutually polarizing charge distributions,

$$\Delta V_{E1}(R) = -\frac{e^2}{2R^4}\left[Z_B^2\alpha_D(A) + Z_A^2\alpha_D(B)\right], \qquad (37)$$

evaluated with the same measured polarizabilities, gives 0.094 MeV at $R = 20$ fm and 0.261 MeV at $R = 15.5$ fm. At the larger separations it agrees with the corrected result to about 10%, the difference being the quadrupole and nuclear terms which Eq. (37) does not contain, while at $R = 15.5$ fm it lies below it by a factor of 1.7. This is to be expected, since by then the nuclear contribution amounts to 37% of the energy for ^{208}Pb and a classical dipole formula cannot represent it. The comparison is thus a check of the rescaling where the dipole dominates and a measure of the nuclear contribution where it does not.

The range given in Table V is the parametric uncertainty of the rescaling. It does not cover the systematic uncertainty of the rescaling itself; that is, of whether the multiplication by $\alpha_D^{\rm expt}/\alpha_D$ is the right way to represent a residual interaction which has not been included; that residual is not quantified here. The uncorrected energy is retained in Table V and in Fig. 11 as a diagnostic of the size of the total correction and not as an endpoint of a physical range. A calculation with the residual interaction, which is the proper remedy, is beyond the scope of the present work.

The change of the mean-square radius is positive but very small, and it is almost entirely a consequence of the displacement of the proton distribution rather than of a breathing of the density. A rigid shift $d_p = |\Delta D_1|/Z$ of the protons raises $\langle r^2\rangle$ by $(Z/A)d_p^2$, which at the larger separations accounts for the whole of the calculated value for ^{208}Pb and for about 60% of it for ^{40}Ca. The estimate ceases to apply for ^{208}Pb once the neutrons begin to respond: it covers 67% of $\Delta\langle r^2\rangle$ at $R = 17$ fm and only 13% at $R = 15.5$ fm, where the increase is no longer a rigid displacement but the leakage of amplitude toward the partner. The effect is very small for ^{208}Pb, where $\Delta\langle r^2\rangle$ reaches only 0.023 fm^2 at $R = 15.5$ fm, corresponding to an increase of the root-mean-square radius by 0.002 fm. For ^{40}Ca the relative effect is larger, 0.033 fm^2 at the same separation, because of the smaller size of the nucleus and of the stronger field of the heavy partner. The particle number is conserved to better than 10^{-3} in all cases, which confirms the numerical accuracy of the calculations.

H. Relevance for the equations of relative motion

In the DNS approach, the polarization of the fragment densities is not included in the equations of relative motion. The nucleus-nucleus potential is constructed from the ground-state densities of the two nuclei, which are kept frozen during

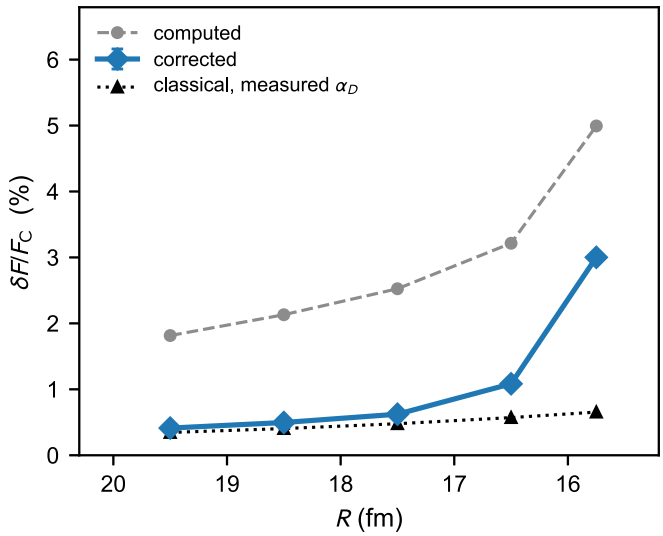


FIG. 11. Change of the radial force, $\delta F = |\partial \Delta V/\partial R|$, as a percentage of the Coulomb force F_C. The three curves correspond to the three energies of Table V, with the same names: the corrected result (full symbols), the computed energy before correction (gray), and the classical estimate of Eq. (37), evaluated with the measured polarizabilities (dotted). The computed curve is retained as a diagnostic of the size of the correction and not as an endpoint of a physical range. Each difference is plotted at the midpoint of the interval over which it is taken.

the approach, and the deformation parameters entering the driving potential are the static ones taken from the tables. This assumption is a natural first approximation, but it has not been verified microscopically, and the size of the correction which it neglects is not known beforehand. One of the purposes of the present calculation is to provide that check.

The magnitudes obtained here can therefore be placed directly against the ingredients of the equations of relative motion [7–9,30]. In that framework the radial coordinate obeys $\mu(R)\ddot{R} = -\partial V/\partial R - \gamma_R(R)\dot{R}$, and the density polarization can in principle enter through the interaction potential $V(R)$, through the radial friction coefficient γ_R, through the coordinate-dependent inertia $\mu(R)$, and through the single-particle spectrum which determines the nucleon transfer rates. Of these, only the first is affected at a level which the present calculation can quantify. The polarization energy of Eq. (24) is the second-order correction to the frozen-density folding potential; it is negative by construction, and it therefore acts as an additional attraction. What matters for the trajectory is not ΔE itself but its radial derivative. That derivative is not constant over the range studied, and neither is the Coulomb force against which it must be weighed, so a single percentage is not meaningful. Evaluated interval by interval, the Coulomb force at the midpoints rises from 6.2 to 9.5 MeV/fm across the range, while $-\partial \Delta V/\partial R$ rises much faster, so that the ratio grows from 0.41% between $R = 20$ and 19 fm to 3.0% between 16 and 15.5 fm under the corrected prescription, with an uncertainty of 0.03 and 0.05 percentage points, respectively. The uncorrected energies would give 1.8% to 5.0% over the same intervals. The full dependence is shown in Fig. 11. The radial friction coefficient is proportional to the squared radial gradients of the single-particle coupling matrix elements [30] and therefore depends on the density change only at second order; with a relative change of the surface density of the order of 10^{-3}, the resulting change of γ_R is negligible in comparison with the uncertainty associated with the one-body treatment of the dissipation [31]. The mass parameter $\mu(R)$ is governed by the overlap integral of the two density distributions and is unaffected at the separations considered here, where that overlap vanishes.

The induced quadrupole deformations, $|\Delta\beta_2| \lesssim 3 \times 10^{-3}$, are small in comparison with the accuracy to which the static deformation parameters entering the driving potential are known. The tabulated β_2 values used in such calculations [26,27] carry uncertainties of the order of 10^{-2}, and the discretization of the grids over the orientation angles of the symmetry axes corresponds to still larger variations of the interaction potential. The quadrupole polarization computed here is therefore not resolvable as a correction to the driving potential, and the frozen deformation treatment of the fragments remains adequate for that purpose. It may be noted that a polarization of the same sign is already generated in trajectory calculations in which the quadrupole amplitudes are propagated as driven oscillators, since the Coulomb driving term $\partial V_C/\partial\beta_2$ is positive and drives the amplitude toward oblate values.

The polarization energy is an additional attraction which is absent from the folded potential, so that the true adiabatic potential lies below the frozen-density one at every separation at which the present calculation applies. Since $|\Delta E|$ increases as the nuclei approach each other, the correction is a steepening of the potential and not a constant shift. If this trend continued inward, it would lower the barrier and move its position slightly outwards, but the calculation stops 2.5 fm outside the barrier and cannot establish that it does; the statement is an implication of the trend and not a result. This is the same qualitative behavior as the energy dependence of the microscopic potentials extracted from TDHF near the barrier [15,16]. It should be noted that the redistribution of the density toward the surface facing away from the partner, which by itself would reduce the overlap of the two distributions and weaken the attractive folding term, is not a separate correction to be set against ΔE, but one of the contributions already contained in it; its size is examined below as a decomposition of ΔE and not as an addition to it. Near the Coulomb barrier, the capture cross section depends exponentially on the barrier height, and a shift of a few hundred keV would be observable in a barrier-distribution measurement. It must be stressed, however, that the present calculation stops at $R = 15.5$ fm, some 2.5 fm outside the barrier, and that a quantitative evaluation of the modified capture cross section is beyond its scope. What can be stated is the scale of the effect at the separations at which the dinuclear system is formed and not its value at the top of the barrier.

The leading adiabatic correction to the frozen-density nucleus-nucleus potential is the polarization energy itself,

$$\Delta V(R) = \Delta E_A(R) + \Delta E_B(R), \tag{38}$$

the two partners contributing additively because each of them is polarized by the frozen field of the other. This is the complete second-order correction and not one term of a sum: the factor of $1/2$ in Eq. (24) already contains the cancellation between the gain in the interaction energy, $\int U_{\rm ext}\delta\rho$, and the cost of the internal rearrangement, $-\frac{1}{2}\int U_{\rm ext}\delta\rho$, so that the change of the interaction produced by the polarized density lies inside ΔE; recomputing the folding integral with $\rho_0+\delta\rho$ and adding the result would count it twice.

The refolding is nevertheless a useful decomposition. Evaluating Eq. (13) with the surfaces deformed by the $\Delta\beta_2$ and $\Delta\beta_3$ of Table III changes $V_{\rm N}$ from -0.0260 to -0.0256 MeV at $R=17$ fm and from -0.2803 to -0.2800 MeV at $R=15.5$ fm; that is, by less than 5×10^{-4} MeV. This covers the nuclear multipole part alone and not the induced Coulomb multipoles, which are much larger; it shows that the shape deformation contributes negligibly to ΔV through the folding integral, the polarization being carried almost entirely by the dipole displacement of the protons in the Coulomb field, as Eq. (34) shows directly.

Numerically, $|\Delta V|$ runs from 0.105 MeV at $R=20$ fm to 0.450 MeV at $R=15.5$ fm under the corrected prescription, against 0.491 and 1.463 MeV as computed; the values and their uncertainties are given in Table V. The associated change of the radial force grows from 0.4% to 3.0% of the Coulomb force between the largest and the smallest separation studied. This is the quantitative answer to the question of how much the frozen-density assumption of the DNS approach neglects in the entrance channel: at the separations at which the dinuclear system is formed, the neglected radial force is a few percent of the Coulomb one at most, and it is well below one percent over most of the range.

Two limitations of Eq. (38) should be kept in mind. It is a second-order correction to a folded potential whose radius parameters have in practice been adjusted to reproduce the measured capture cross sections, so that it cannot simply be added to such a potential without recalibrating it; the consistent alternative is to use the microscopic result in order to constrain the stiffness of a dynamical deformation degree of freedom. It is also established only outside $R=15.3$ fm, whereas the barrier of the ^{40}Ca + ^{208}Pb system lies near $R\simeq13$ fm, where both parts of the external field are considerably larger. The extrapolation of ΔV to the barrier is not attempted here.

The situation is different for the dipole component of the response. It dominates the polarization energy over the whole range of separations studied, and the DNS interaction potential contains no corresponding degree of freedom, so that this contribution is absent from the model rather than small within it. It is the direct analog of the adiabatic Coulomb polarization potential known from elastic scattering [17,18], whose classical form $\Delta V=-\alpha_D Z_B^2e^2/2R^4$ reproduces the nearly constant polarizability extracted in Sec. IV G. Its magnitude at the barrier cannot be established here. The present calculation is restricted to $R\geqslant15.5$ fm, whereas the barrier of the ^{40}Ca + ^{208}Pb system is located near $R\simeq13$ fm, and both parts of the external field grow rapidly between these two distances. A quantitative statement about the capture cross section would require a two-center treatment in the barrier region, together with the removal of the center-of-mass component of the dipole response discussed in Sec. IV G. The present results should accordingly be regarded as establishing the scale of the effect rather than as a quantitative modification of the entrance-channel potential. That scale, a few hundred keV at $R\simeq15.5$ fm, is comparable to the spread produced by the different radius parametrizations in use for the folding potential, and it is therefore in part already absorbed in the empirical calibration of that potential.

The conclusion of this section is thus that for two spherical partners, and at the separations at which the present calculation is applicable, the neglect of the density polarization in the equations of relative motion is justified: the induced quadrupole deformation lies below the precision to which the static deformations are known, and the associated change of the radial force amounts to a few percent. It should be stressed that this conclusion is specific to the case examined here. The induced deformation grows as the separation decreases, and it is expected to be larger for statically deformed partners, where the surfaces approach each other more closely in the tip orientation. Should the induced deformation in those cases prove to be comparable with the accuracy of the tabulated β_2 values, it would have to be included explicitly in the equations of relative motion, either as an additional degree of freedom propagated alongside $R(t)$ or through a polarization correction to the interaction potential. The verification of this point for deformed nuclei and at separations closer to the barrier is left to future work.

V. CONCLUSIONS

The polarization of the nucleon density of ^{208}Pb and ^{40}Ca in the dinuclear configuration has been calculated microscopically by rediagonalizing the deformed Woods–Saxon single-particle problem with the combined Coulomb and DNS-consistent folded nuclear field of the partner nucleus, and the induced density change has been obtained explicitly and decomposed into its Coulomb and nuclear parts. The double-folding and frozen Hartree-Fock descriptions [8,11,12] keep the densities frozen and do not contain this correction; TDHF and DC-TDHF [13,15,16] contain it dynamically but yield the potential of the composite system rather than the response of one partner, and do not separate the two components of the external field. The external field consists of the Coulomb potential of the partner and of the nuclear potential obtained by double folding of the Migdal density-dependent interaction, taken in the same form as in the DNS approach, so that the polarization is consistent with the potential which governs the relative motion.

The induced density change is localized in the surface region of both nuclei. It is dominated by the repulsive Coulomb tidal field, which compresses the density along the internuclear axis and produces a negative induced quadrupole moment. The nuclear part of the external field acts in the opposite direction, but because the Migdal force has zero range, this contribution becomes appreciable only when the surfaces of the two nuclei approach each other. As a result, the modulus of ΔQ_{20} passes through a maximum at $R\simeq17$ fm for

^{208}Pb and at $R \simeq 16$ fm for ^{40}Ca, and no change of sign occurs within the range of separations accessible to the one-center description. An extrapolation of the exponential growth of the nuclear contribution places that change of sign near $R \simeq 15$ fm, so that a prolate polarization is to be expected in the barrier region itself. The Coulomb part of the response follows the R^{-3} tidal law over the whole range. Expressed through the deformation parameter, the induced quadrupole deformations are of the order of 10^{-3}, and at the larger separations the induced octupole deformations are close to 40% of them for ^{208}Pb and to 50% for ^{40}Ca. The lighter partner is the more strongly polarized of the two in relative terms, $\Delta\beta_2$ of ^{40}Ca being between two and three times that of ^{208}Pb at every separation, although its induced quadrupole moment is seven times smaller in absolute value. The polarization energy of the system at $R = 15.5$ fm is 1.46 MeV in magnitude as computed and 0.45 ± 0.02 MeV once the spurious translational part of the Coulomb dipole response has been removed and that component screened to the measured polarizability. The correction is applied to the dipole component alone, which carries 62% to 99% of the energy depending on the separation and on the partner; the quadrupole and nuclear contributions are left as computed.

The moments have to be taken about the center of mass of the density and not about the fixed center of the mean field. A displaced but undeformed distribution acquires a quadrupole moment $2N_q d^2$ about a fixed origin, and in the present problem this kinematic term is comparable with the induced moment itself. Evaluated in the laboratory frame, the rediagonalized and the first-order quadrupole moments appear to differ by 6% for ^{208}Pb and by 45% for ^{40}Ca at $R = 20$ fm, and almost the whole of the first difference and about three-quarters of the second are accounted for by that term. In the intrinsic frame, the response of ^{208}Pb agrees with the first-order one to better than half a percent down to $R = 17$ fm, and it does so over the full range of the switching parameter for the Coulomb field at $R = 20$ fm, while the genuine higher-order contribution for ^{40}Ca is 12% to 16% and not 45%, a figure which is not yet converged with the size of the basis and is more likely to grow than to shrink. The polarization energy, which is carried by the dipole channel, is well represented by its second-order expression, the coupling-constant integration reproducing it to better than 1% in eleven of the twelve configurations computed, the exception being ^{208}Pb at the edge of the domain of validity.

A quantitative criterion for the validity of the one-center approximation has also been established, which does not appear to have been formulated previously for this class of calculation. The description remains valid as long as the barrier separating the two single-particle wells lies above the Fermi level, Eq. (31), which for the $^{40}\mathrm{Ca} + {}^{208}\mathrm{Pb}$ system corresponds to $R > 15.3$ fm. Below this distance, the barrier between the two single-particle wells disappears, nucleons are transferred to the partner, and the result does not converge with the size of the basis. Since the touching configuration of this system lies at $R \simeq 12.1$ fm, the region of the interaction potential which is most important for the capture process is not accessible to a one-center calculation, and a two-center basis is required. In the DNS approach, the fragment densities are kept frozen, and the polarization is not included in the equations of relative motion. The present calculation provides a check of that assumption, which has so far been missing. For two spherical partners, and at the separations at which the one-center description is applicable, the neglect is justified, since the induced quadrupole deformation is smaller than the uncertainty of the tabulated static deformations and the associated change of the radial force is of the order of a few percent. This result is specific to the case studied here. If for deformed partners, or at separations closer to the barrier, the induced deformation is found to be comparable with that uncertainty, it should be taken into account explicitly in the equations of relative motion in future work.

The present study has been restricted to two spherical partners. This choice isolates the induced polarization from the static deformation of the ground state and makes it possible to establish the method and the conditions of its applicability. The natural continuation is the treatment of statically deformed nuclei, for which two new effects are expected. First, the external field acting on a deformed partner depends on the orientation of its symmetry axis relative to the internuclear axis. For a prolate partner, the surfaces come closer at a given R in the tip orientation, and since the nuclear part of the external field varies over the short length scale of the density diffuseness, it is the nuclear contribution rather than the Coulomb one that is strongly orientation dependent. The polarization energy is therefore expected to be larger in the tip orientation, whereas the induced quadrupole moment may well be smaller there, because the prolate nuclear contribution then cancels more of the oblate Coulomb one. The separation at which the sign of ΔQ_{20} changes should accordingly move outwards in the tip orientation. Second, the induced deformation adds to the static one and may either increase or reduce the effective deformation entering the driving potential, depending on the sign of the ground-state β_2. Since the deformation parameters of the fragments and their orientations are among the main quantities determining the capture and quasifission probabilities in the DNS approach [9,32], the polarization corrections to them are of direct interest, and their calculation is planned as the next step of this work.

ACKNOWLEDGMENT

The author is grateful to A. K. Nasirov for valuable discussions.

DATA AVAILABILITY

There are no publicly available research data or software supporting this paper. Requests for further information or data should be sent to the author.

[1] S. Hofmann and G. Münzenberg, The discovery of the heaviest elements, Rev. Mod. Phys. **72**, 733 (2000).

[2] S. A. Giuliani, Z. Matheson, W. Nazarewicz, E. Olsen, P.-G. Reinhard, J. Sadhukhan, B. Schuetrumpf, N. Schunck, and P. Schwerdtfeger, *Colloquium*: Superheavy elements: Oganesson and beyond, Rev. Mod. Phys. **91**, 011001 (2019).

[3] N. V. Antonenko, E. A. Cherepanov, A. K. Nasirov, V. P. Permjakov, and V. V. Volkov, Compound nucleus formation in reactions between massive nuclei: Fusion barrier, Phys. Rev. C **51**, 2635 (1995).

[4] G. G. Adamian, N. V. Antonenko, and W. Scheid, Isotopic dependence of fusion cross sections in reactions with heavy nuclei, Nucl. Phys. A **678**, 24 (2000).

[5] B. M. Kayumov, O. K. Ganiev, A. K. Nasirov, and G. A. Yuldasheva, Analysis of the fusion mechanism in the synthesis of superheavy element 119 via the ^{54}Cr + ^{243}Am reaction, Phys. Rev. C **105**, 014618 (2022).

[6] A. Nasirov and B. Kayumov, Optimal colliding energy for the synthesis of a superheavy element with $Z = 119$, Phys. Rev. C **109**, 024613 (2024).

[7] B. Kayumov, Investigation of the formation of superheavy elements with atomic numbers 116 and 120 through ^{50}Ti-induced reactions, Phys. Rev. C **111**, 054619 (2025).

[8] G. G. Adamian, N. V. Antonenko, R. V. Jolos, S. P. Ivanova, and O. I. Melnikova, Effective nucleus-nucleus potential for calculation of potential energy of a dinuclear system, Int. J. Mod. Phys. E **5**, 191 (1996).

[9] A. Nasirov, A. Fukushima, Y. Toyoshima, Y. Aritomo, A. Muminov, S. Kalandarov, and R. Utamuratov, The role of orientation of nucleus symmetry axis in fusion dynamics, Nucl. Phys. A **759**, 342 (2005).

[10] V. Y. Denisov and W. Nörenberg, Entrance channel potentials in the synthesis of the heaviest nuclei, Eur. Phys. J. A **15**, 375 (2002).

[11] G. R. Satchler and W. G. Love, Folding model potentials from realistic interactions for heavy-ion scattering, Phys. Rep. **55**, 183 (1979).

[12] D. T. Khoa and G. R. Satchler, Generalized folding model for elastic and inelastic nucleus–nucleus scattering using realistic density dependent nucleon–nucleon interaction, Nucl. Phys. A **668**, 3 (2000).

[13] C. Simenel and A. S. Umar, Heavy-ion collisions and fission dynamics with the time-dependent Hartree–Fock theory and its extensions, Prog. Part. Nucl. Phys. **103**, 19 (2018).

[14] C. Simenel, Nuclear quantum many-body dynamics, Eur. Phys. J. A **48**, 152 (2012).

[15] A. S. Umar and V. E. Oberacker, Heavy-ion interaction potential deduced from density-constrained time-dependent Hartree-Fock calculation, Phys. Rev. C **74**, 021601(R) (2006).

[16] K. Washiyama and D. Lacroix, Energy dependence of the nucleus-nucleus potential close to the Coulomb barrier, Phys. Rev. C **78**, 024610 (2008).

[17] A. J. Baltz, N. K. Glendenning, S. K. Kauffmann, and K. Pruess, Long range absorption and other optical-model effects from strong inelastic coupling, Nucl. Phys. A **327**, 221 (1979).

[18] K. Alder and A. Winther, *Electromagnetic Excitation* (North-Holland, Amsterdam, 1975).

[19] S. Ćwiok, J. Dudek, W. Nazarewicz, J. Skalski, and T. Werner, Single-particle energies, wave functions, quadrupole moments and g-factors in an axially deformed Woods–Saxon potential with applications to the two-centre-type nuclear problems, Comput. Phys. Commun. **46**, 379 (1987).

[20] A. B. Migdal, *Theory of Finite Fermi Systems and Applications to Atomic Nuclei*, 2nd ed. (Nauka, Moscow, 1983).

[21] P. Ring and P. Schuck, *The Nuclear Many-Body Problem* (Springer Berlin Heidelberg, Berlin, 1980).

[22] I. Angeli and K. P. Marinova, Table of experimental nuclear ground state charge radii: An update, At. Data Nucl. Data Tables **99**, 69 (2013).

[23] H. de Vries, C. W. de Jager, and C. de Vries, Nuclear charge-density-distribution parameters from elastic electron scattering, At. Data Nucl. Data Tables **36**, 495 (1987).

[24] M. Wang, W. J. Huang, F. G. Kondev, G. Audi, and S. Naimi, The AME 2020 atomic mass evaluation (II). Tables, graphs and references, Chin. Phys. C **45**, 030003 (2021).

[25] D. Adhikari, H. Albataineh, D. Androic, K. Aniol, D. S. Armstrong, T. Averett, C. Ayerbe Gayoso, S. Barcus, V. Bellini, R. S. Beminiwattha, J. F. Benesch, H. Bhatt, D. Bhatta Pathak, D. Bhetuwal, B. Blaikie, Q. Campagna, A. Camsonne, G. D. Cates, Y. Chen, C. Clarke, *et al.*, Accurate determination of the neutron skin thickness of ^{208}Pb through parity-violation in electron scattering, Phys. Rev. Lett. **126**, 172502 (2021).

[26] S. Raman, C. W. Nestor Jr., and P. Tikkanen, Transition probability from the ground to the first-excited 2^+ state of even–even nuclides, At. Data Nucl. Data Tables **78**, 1 (2001).

[27] P. Möller, J. R. Nix, W. D. Myers, and W. J. Swiatecki, Nuclear ground-state masses and deformations, At. Data Nucl. Data Tables **59**, 185 (1995).

[28] A. Tamii, I. Poltoratska, P. von Neumann-Cosel, Y. Fujita, T. Adachi, C. A. Bertulani, J. Carter, M. Dozono, H. Fujita, K. Fujita, K. Hatanaka, D. Ishikawa, M. Itoh, T. Kawabata, Y. Kalmykov, A. M. Krumbholz, E. Litvinova, H. Matsubara, K. Nakanishi, R. Neveling, *et al.*, Complete electric dipole response and the neutron skin in ^{208}Pb, Phys. Rev. Lett. **107**, 062502 (2011).

[29] R. W. Fearick, P. von Neumann-Cosel, S. Bacca, J. Birkhan, F. Bonaiti, I. Brandherm, G. Hagen, H. Matsubara, W. Nazarewicz, N. Pietralla, V. Y. Ponomarev, P.-G. Reinhard, X. Roca-Maza, A. Richter, A. Schwenk, J. Simonis, and A. Tamii, Electric dipole polarizability of ^{40}Ca, Phys. Rev. Res. **5**, L022044 (2023).

[30] G. G. Adamian, R. V. Jolos, A. K. Nasirov, and A. I. Muminov, Friction coefficient for deep-inelastic heavy-ion collisions, Phys. Rev. C **56**, 373 (1997).

[31] J. Randrup and W. J. Swiatecki, Dissipative resistance against changes in the mass asymmetry degree of freedom in nuclear dynamics: The completed wall-and-window formula, Nucl. Phys. A **429**, 105 (1984).

[32] A. K. Nasirov, A. R. Yusupov, and B. M. Kayumov, Small cross section of the synthesis of darmstadtium in the ^{48}Ca+^{232}Th reaction, Phys. Rev. C **110**, 014618 (2024).